Helsinki University of Technology
Inorganic Chemistry Publication Series
Espoo 2007 No. 8

SYNTHESIS AND CHARACTERIZATION OF SOME RUDDLESDEN-POPPER AND SPINEL TYPE OXIDES

Mikko Matvejeff

Dissertation for the degree of Doctor of Science in Technology to be presented with due permission of the Department of Chemical Technology for public examination and debate in Auditorium Ke2 at Helsinki University of Technology (Espoo, Finland) on the 2nd of November, 2007, at 12 noon.

Helsinki University of Technology
Department of Chemical Technology
Laboratory of Inorganic and Analytical Chemistry

Teknillinen korkeakoulu
Kemian tekniikan osasto
Epäorgaanisen ja analyyttisen kemian laboratorio

Distribution:
Helsinki University of Technology
Laboratory of Inorganic and Analytical Chemistry
P.O. Box 6100
FI-02015 TKK, FINLAND
E-mail: Mikko.Matvejeff@iki.fi

ISBN 978-951-22-9002-4
ISBN 978-951-22-9007-9 (PDF)
ISSN 1458-5154

Picaset Oy
Helsinki 2007

ABSTRACT

The present thesis consists of six publications and a summary of the experimental results reviewed together with relevant literature data. Two transition metal oxide (TMO) systems were investigated: $Sr_2Q_{n-1}B_2O_{3n+1-\delta}$ (Q = Y, Ca, Sr; B = Co, Fe; n = 1, 2, 3 and ∞) compounds with a Ruddlesden-Popper (RP) crystal structure and the $InFeMO_4$ (M = Mg, Co, Ni, Cu and Zn) compounds with a spinel structure (for Mg, Co and Ni). For both systems, polycrystalline samples were synthesized and characterized for magnetic and (magneto)transport properties which were then interpreted in terms of the site-specific cation composition, oxygen content and the oxidation state of the transition metal species.

The interplay between oxygen stoichiometry and structural properties was studied for the RP oxides, $Sr_2(Ca,Y)Co_2O_{7-\delta}$. It was shown that the maximum value of oxygen content significantly depends on the average valence of the (Y,Ca)-site cations, increasing with increasing Y^{III}-for-Ca^{II} substitution level. The strong impact of oxygen content on transport properties was confirmed, as the highly oxygenated samples exhibited significantly lower resistivity (by several decades) compared to the oxygen-depleted samples. In addition, concentration of oxygen vacancies in the (Ca,Y)O layer was observed to have a large effect on the magnetic properties, as filling the vacancies facilitated the emergence of ferromagnetic order and increased the strength of the magnetoresistance (MR) effect.

The tendency of the RP oxides to absorb additional layers of water was studied for the $Sr_{n+1}Fe_nO_{3n+1-\delta}$ series (n = 1, 2, 3 and ∞) by subjecting the samples to humidity under carefully controlled conditions. In addition, the intercalation reaction was also studied under extreme exposure by directly immersing some samples into distilled water. As result, novel layered water-derivative phases were obtained and identified by means of powder XRD measurements. The importance of the $(SrO)_2$ double layer of rock-salt structure was demonstrated, as it was shown that the n = ∞ member lacking the layer

did not absorb water. Moreover, it was revealed that the rate of the derivative-phase formation depends on *n* and also on the concentration of oxygen vacancies.

The narrow overall cation composition ranges and the distribution of each cation species between the two cation sites in the InFe*M*O_4 (*M* = Mg, Co, Ni, Cu and Zn) system were studied by means of ICP measurements and Rietveld refinement of powder XRD data. The impacts of cation stoichiometry and magnetic dilution on the magnetic properties were investigated as well. In addition, a novel fitting method for the Mössbauer spectra of the cation-disordered spinel phases was developed in order to more accurately determine the cation distribution, iron oxidation state and magnetic order in these phases.

PREFACE

The experimental work for this thesis has been carried out in the Laboratory of Inorganic and Analytical Chemistry at Helsinki University of Technology (TKK) and Yamauchi-Karppinen Group, Materials and Structures Laboratory, Tokyo Insitute of Technology (TokyoTech) between January 2002 and April 2007. The work is part of a currently ongoing collaboration project between TKK and TokyoTech and earlier phases of this work have been published in a Licentiate of Technology thesis approved in September 2004.

I wish to extend my deepest thanks to my supervisor Prof. Maarit Karppinen (TKK) for all the advice and guidance I have received during my studies. I'm also deeply grateful for Prof. Hisao Yamauchi (TokyoTech) for making it possible for me to work as a part of an inspiring and internationally highly acclaimed research group during the last 7 years.

I'm also deeply indebted to my co-authors for their input, especially to Dr. Johan Lindén from Åbo Academi University for his expert guidance with Mössbauer spectroscopy and generally helpful comments on other aspects of my research as well. To Dr. Markus Valkeapää from TKK I give my most sincere thanks for his invaluable help with the Rietveld refinements and for sharing many memorable moments in Japan in 2004-2006. Dr. Yun-Hui Huang, Mr. Matti Lehtimäki and Ms. Kirsi Salomäki I would like to thank for their invaluable contribution with a project focused on layered RP compounds.

I also wish to express my thanks to Dr. Teruki Motohashi, Dr. Yukiko Yasukawa, Dr. Hiroshi Okamoto, Dr. Jin Nakamura, Dr. Inga Grigoraviciute and Mr. Atsushi Hirasa from Materials and Structures Laboratory for successful collaboration and help with all practical things during my visits to TokyoTech in 2000-2007. Additionally I'm thankful to the personnel both in the Laboratory of Inorganic and Analytical Chemistry at TKK and Yamauchi-Karppinen Group at TokyoTech for creating a productive and supportive working atmosphere.

Finally I wish to warmly thank my family, especially my wife Joanna, for their support, encouragement and patience during the whole project.

Finnish Cultural Foundation, Scandinavia-Japan Sasakawa Foundation, Komppa Foundation and Japan Society for the Promotion of Science (JSPS) are also gratefully acknowledged for financial support.

Tokyo, September 2007

Mikko Matvejeff

LIST OF PUBLICATIONS

In addition to the present review, this thesis includes the following publications (I-VI), which are referred to in the text by their corresponding Roman numerals. The original publications are found in appendices I - VI.

I. M. Karppinen, M. Matvejeff, K. Salomäki and H. Yamauchi, Oxygen Content Analysis of Functional Perovskite-Derived Cobalt Oxides, *J. Mater. Chem.* **12** (2002) 1761-1764.

II. M. Matvejeff, J. Nakamura, H. Yamauchi and M. Karppinen, Oxygen Nonstoichiometry and Magnetotransport Properties of $Sr_2(Y_{1-x}Ca_x)Co_2O_{7+\delta}$ Cobalt Oxides, *Mater. Chem. Phys.* **85** (2004) 329-333.

III. M. Matvejeff, M. Lehtimäki, A. Hirasa, Y.-H. Huang ,H. Yamauchi and M. Karppinen, New Water-Containing Phase Derived from the $Sr_3Fe_2O_{7-\delta}$ Phase with Ruddlesden-Popper Structure, *Chem. Mater.* **17** (2005) 2775-2779.

IV. M. Lehtimäki, A. Hirasa, M. Matvejeff, H. Yamauchi and M. Karppinen, Water Derivatives of the $Sr_{n+1}Fe_nO_{3n+1-\delta}$ Series, *J. Solid State Chem.*, In Press.

V. M. Matvejeff, J. Lindén, M. Karppinen and H. Yamauchi, Studies on $InFeMO_4$ (M = Mg, Co, Ni, Cu and Zn) Compounds: Crystal Structure and Cation Distribution, *J. Solid State Chem.* **180** (2007) 2316-2322.

VI. M. Matvejeff, J. Lindén, T. Motohashi, M. Karppinen and H. Yamauchi, Magnetic Properties of Spinel Oxides, $InFeMO_4$ (M = Mg, Co and Ni), *Solid State Comm.* **144** (2007) 249-254.

THE AUTHOR'S CONTRIBUTION

Publication **I**	Author synthesized and analyzed the oxygen content of the $Sr_2(Y_{0.7}Ca_{0.3})Co_2O_{7-\delta}$ samples. Author had a minor role in writing the manuscript.
Publication **II**	Author defined the research plan together with Prof. M. Karppinen. Author synthesized and characterized the samples. Results were interpreted with the co-authors. Author had a major role in writing the manuscript.
Publications **III** and **IV**	Author defined the research plan together with Prof. M. Karppinen. Author synthesized and characterized the $n = 2$ member of the $Sr_{n+1}Fe_nO_{3n+1-\delta}$ series. Author had a major role in writing the manuscript **III** and participated in writing the manuscript **IV**.
Publications **V** and **VI**	Author defined the research plan, synthesized the samples and performed the characterizations. Analysis of the results from Mössbauer measurements was performed together with Dr. J. Lindén. Author also contributed to the development of the new fitting model for the Mössbauer spectra of $InFeMO_4$ spinel oxides. Author had a leading role in writing the manuscripts.

LIST OF ABBREVIATIONS

Abbreviations in chemical formulas and crystal structures

A	Atomic site/cation in Ruddlesden-Popper and spinel oxides
B	Atomic site/cation in Ruddlesden-Popper and spinel oxides
Q	Atomic site/cation located between BO_2 layers in Ruddlesden-Popper oxides
M	Metal cation
n	Number of BO_2 layers in Ruddlesden-Popper oxides
RE	Rare earth element
x	Degree of inversion in mixed spinel oxides
X	Halogen
δ	Overall oxygen nonstoichiometry *per* formula unit in layered transition metal oxides

Other abbreviations

AFM	Antiferromagnet or antiferromagnetic
CMR	Colossal magnetoresistance
DE	Double exchange
EFG	Electric field gradient
FM	Ferromagnet or ferromagnetic
ICP-OES	Inductively coupled plasma – optical emission spectroscopy
IS	Isomer shift

J_{AA}	Magnetic exchange interaction between *A* cations in spinel oxides
J_{AB}	Magnetic exchange interaction between *A* and *B* cations in spinel oxides
J_{BB}	Magnetic exchange interaction between *B* cations in spinel oxides
MR	Magnetoresistance
NPD	Neutron powder diffraction
P	Paramagnetic
Q	Nuclear quadrupole moment
QCC	Quadrupole coupling constant
RP	Ruddlesden-Popper
RT	Room temperature
SG	Spin glass
T_c	Critical temperature of superconductivity
T_C	Curie temperature, *i.e.* critical temperature of ferromagnetic or ferrimagnetic ordering
TE	Thermoelectricity
TG	Thermogravimetry
TMO	Transition metal oxide
T_N	Néel temperature, *i.e.* critical temperature of antiferromagnetic ordering
XRD	X-ray diffraction

CONTENTS

1. INTRODUCTION

The current interest in layered transition metal oxides (TMOs) originates from the discovery of high-T_c superconductivity in the $(La,Ba)_2CuO_{4-\delta}$ system by Bednorz and Müller two decades ago in 1986 [1]. The discovery attracted considerable attention as superconductivity had previously been observed mainly in pure metals and alloys with their critical temperatures of superconductivity (T_c) located near the boiling point of liquid helium. As a result an extensive research effort was directed towards producing new and improved superconductive phases through chemical substitutions in the original $(La,Ba)_2CuO_{4-\delta}$ system, which led to discoveries of hundreds of structurally related oxide phases.

Since the discovery of Bednorz and Müller, the layered TMOs have become one of the most extensively studied groups of materials in the field of modern materials science. In addition to the large number of superconductive copper oxides, the research has led to the emergence of a wide variety of oxide phases exhibiting other interesting magnetic and electric properties, such as colossal magnetoresistance (CMR) in perovskite manganese oxides [2-7] and high-efficiency thermoelectricity (TE) in layered cobalt oxides [8-12]. In some cases several of these phenomena have simultaneously been observed in a single phase as is the case with the $RuSr_2GdCu_2O_{8-\delta}$ and $RuSr_2(Gd_{0.75}Ce_{0.25})_2Cu_2O_{10-\delta}$ magnetosuperconductors which exhibit simultaneous magnetic ordering and superconductivity [13-16]. Due to their inherent potential the layered TMOs are regarded as promising candidates for many practical applications such as high performance power conversion and transport, magnetic data storage (computer hard drives *etc.*) and spin-selective transistors.

The transition from theory to practical applications has not, however, been an easy one. The functional properties of layered TMOs are often sensitive to small variations in both transition metal oxidation state and local coordination. Well known examples include the link between the mixed oxidation state of copper ($Cu^{II/III}$) [17] and superconductivity properties in high-T_c copper oxides and the importance of the mixed

oxidation states, $Mn^{III/IV}$ [18,19], $Co^{II/III/IV}$ [18,20] and $Fe^{II/III/IV/V}$ [21,22] in CMR oxides, whereas the local coordination plays a crucial role for example in determining the magnetic properties of the half-metallic double-perovskite Sr_2FeMoO_6 [23] and also those of spinel oxides [24-26].

The oxidation state and local coordination of transition metal atoms in layered TMOs are usually controlled by adjusting the overall cation composition or the concentration and/or distribution of oxygen vacancies/excess oxygen. However, the oxidation state and the local coordination of a transition metal in a layered TMO are interrelated and changes, for example in oxygen vacancy concentration or cation composition, often affect both of them simultaneously. Due to this the mechanisms governing the interplay between chemical composition, oxygen content and the resultant functional properties are often not well understood and merit further attention to fully realize the potential of these versatile materials.

Ruddlesden-Popper (RP) oxides tend to exhibit high flexibility in terms of cation composition and oxygen content. As such they are good candidates for studying the effect of cation composition and oxygen content on various functional properties. In this thesis $Sr_2(Y,Ca)Co_2O_{7-\delta}$ oxides of the RP structure were synthesized with selected Y/Ca ratios and oxygen vacancy concentrations in order to probe the dependencies between chemical composition, oxygen nonstoichiometry and magnetotransport properties [**I**,**II**].

In addition, RP oxides of Co [27-29], Cu [30-32], Zr [33], Ti [34] and Fe [35,**III**,**IV**] may absorb water to form derivative phases when subjected to ambient humidity. This behavior has been attributed to the presence of highly oxidized transition metal species in the structure. In this thesis the formation of the layered derivatives were studied for the $Sr_{n+1}Fe_nO_{3n+1-\delta}$ (n = 1, 2, 3 and ∞) series [**III,IV**] by correlating the structural properties, oxygen vacancy concentration and oxidation state of iron with the formation rate and stability of the derivative phases.

Unlike the perovskite-derived structures, the spinel oxides are usually highly resistant to changes in oxygen content. This facilitates the study of cation substitution and distribution effects without the interference arising from the changes in the oxygen vacancy concentration. In this thesis the phase formation and the effect of identity of

cation *M* and level of magnetic dilution on the magnetic properties were studied in the $InFeMO_4$ (*M* = Mg, Co and Ni) spinel oxide system.

2. RUDDLESDEN-POPPER AND SPINEL OXIDES

The interesting functional properties of layered TMOs are directly related to the complex crystal structure and flexibility in terms of cation and oxygen content encountered in these phases. In this chapter, the crystal structures of RP and spinel oxides are discussed in detail, followed by a short introduction to the roles of cation composition and distribution. In addition, the methods employed in the characterization of these properties, *i.e.* plasma emission spectroscopy (Inductively Coupled Plasma-Optical Emission Spectroscopy, ICP-OES), Rietveld refinement and Mössbauer spectroscopy, are briefly introduced.

2.1. Ruddlesden-Popper structure

The ideal RP structure of $A_2Q_{n-1}B_nO_{3n+1-\delta}$ is closely related to the basic perovskite structure as it is based on a perovskite-structured block, $Q_{n-1}B_nO_{3n-1}$ ($n \geq 1$), consisting of n-1 QO layers and n BO_2 layers. This block is sandwiched between two rock-salt-structured AO layers according to the layer sequence of AO-BO_2-(QO-BO_2)$_{n-1}$-AO. The δ in the formula, $A_2Q_{n-1}B_nO_{3n+1-\delta}$, denotes the degree of oxygen nonstoichiometry and will be discussed in detail later.

The structural similarity of perovskite and RP structures is illustrated in Figure 1 showing the structures of $A_2Q_{n-1}B_nO_{3n+1-\delta}$ for n = 1, 2, 3 and ∞ (*i.e.* the perovskite structure). The RP phases are derived from the parent perovskite phase by the addition of one extra AO layer, leading to a transition in the *ab* plane between two consecutive unit cells. Due to the transition in [110] direction, the unit cell of the ideal RP structure consists of two formula units and possesses tetragonal symmetry (space group $I4/mmm$) with an elongated *c* axis instead of the cubic unit cell of the ideal perovskite structure (space group $Pm3m$).

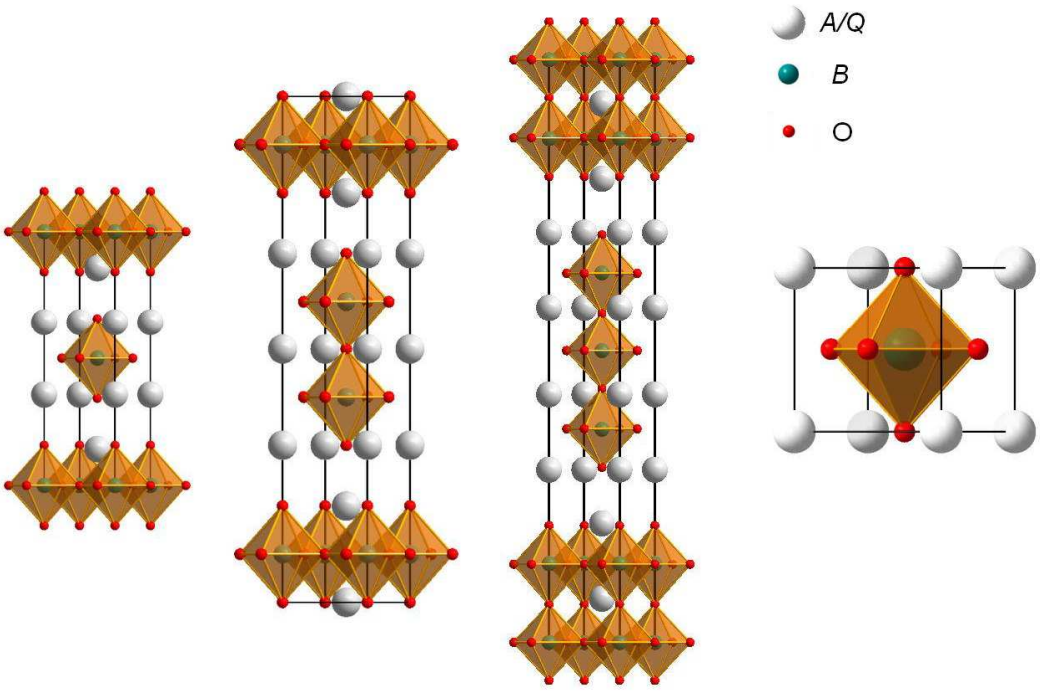

Figure 1: Comparison of oxygen-stoichiometric $n = 1$ (A_2BO_4), $n = 2$ ($A_2QB_2O_7$), $n = 3$ ($A_3QB_3O_{10}$) and $n = \infty$ (perovskite, ABO_3) ideal RP structures. The unit cell of each structure is presented by a black rectangle. Figure drawn based on the data from Bilbao crystallographic server and reference [36].

Since the discovery of the first RP compounds, $Sr_2TiO_{4-\delta}$, $Ca_2MnO_{4-\delta}$ and $(Sr_{0.5}La_{0.5})_2AlO_{4-\delta}$ [37], a large number of RP phases have been synthesized as the RP structure is highly flexible in terms of the cation composition both at the *A*/*Q* and the *B* sites (see Table 1). The *A* and *Q* sites are usually occupied by alkaline, alkaline earth or rare earth elements of widely varying sizes, whereas the *B* site is usually occupied by a transition metal, although other *B*-site constituents such as Li and In [38,39] have also been reported. Preparation of oxyhalogenides through partial substitution of oxygen by a halogen element has been demonstrated as well, initially for Cu [40-42] and later for other transition metals as well [43-47].

The known phases can be classified as members of so-called homologous series. A homologous series is defined as a family of phases where only the number of BO_2 layers (n) in the infinite-layer block, $Q_{n-1}B_nO_{3n-1}$, changes. Examples of RP homologous series for various transition metals, *B*, are given in Table 1.

Table 1: Examples of homologous series of $A_2Q_{n-1}B_n(O,X)_{3n+1-\delta}$ RP oxides where $1 \leq n \leq 3$. *X* in the chemical formula denotes halogen element.

B	*n = 1*	*n = 2*	*n = 3*
Mn			
	Sr_2MnO_4 [48]	$Sr_3Mn_2O_7$ [49]	$Sr_4Mn_3O_{10}$ [50]
	Ca_2MnO_4 [51]	$Ca_3Mn_2O_7$ [51]	$Ca_4Mn_3O_{10}$ [50]
	$(La,Sr)_2MnO_4$ [48,52]	$(La,Sr)_3Mn_2O_7$ [53]	
	Sr_2MnO_3Cl [46]		$Sr_4Mn_3O_8Cl_2$ [46]
Fe			
	Sr_2FeO_4 [54,55, **IV**]	$Sr_3Fe_2O_7$ [55,58, **III**,**IV**]	$Sr_4Fe_3O_{10}$ [58,**IV**]
	Sr_2FeO_3X [56]	$Sr_3Fe_2O_5X_2$ [59]	
	$(La,Sr)_2FeO_4$ [57]	$(La,Sr)_3Fe_2O_7$ [57]	$(La,Sr)_4Fe_3O_{10}$ [57]
Co			
	Sr_2CoO_4 [60-62]	$Sr_3Co_2O_7$ [60,65]	$Sr_4Co_3O_{10}$ [60]
	La_2CoO_4 [63,64]		$La_4Co_3O_{10}$ [36,63]
	Nd_2CoO_4 [64]	$Sr_2(Y,Ca)Co_2O_7$ [66, **II**]	$Nd_4Co_3O_{10}$ [67]
	Sr_2CoO_3Cl [45]	$Sr_3CoO_5Cl_2$ [45]	
Ni			
	$(La,Sr)_2NiO_4$ [68-70]	$(La,Sr)_3Ni_2O_7$ [69,70,72,73]	$(La,Sr)_4Ni_3O_{10}$ [69,70,74-76]
	Nd_2NiO_4 [71]		$Nd_4Ni_3O_{10}$ [67]

2.2. Spinel structure

The perovskite-derived structures are in general rather flexible in terms of oxygen stoichiometry. Moreover, the flexibility in oxygen content often allows a high degree of variation in chemical composition as well. In contrast, the spinel structure is usually highly resistant to changes in oxygen content and accordingly exhibits less variety both in terms of possible cation compositions and transition metal oxidation state(s).

The ideal spinel structure has a cubic symmetry with space group $Fd\bar{3}m$. In the spinel structure the divalent *A* cations occupy 1/8 of the tetrahedral sites with T_d symmetry, trivalent *B* cations occupy 1/2 of the octahedral sites with D_{3d} symmetry and the oxygen anions are arranged in a cubic close-packed structure. The unit cell consists of 8 formula units and can be presented as a large lattice where two types of cubic building blocks, AO_4 and B_4O_4, alternately fill up the 8 octants as shown in Figure 2.

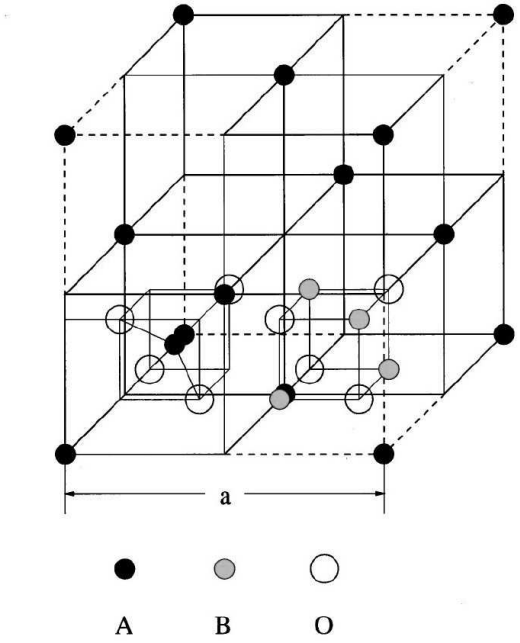

Figure 2: Crystal structure of spinel, AB_2O_4. For clarity, only two octants of the spinel are filled. Other octants are occupied alternately by the tetrahedral (octant without dashed line) and octahedral (octant with dashed lines) units [77].

In addition to the ideal spinel structure, where the divalent cations occupy *A* sites and trivalent cations occupy *B* sites, so-called inverse spinels are also known. In the inverse spinel structure half of the *B* cations reside in tetrahedral positions, while equal amounts of *A* and *B* cations are found in the octahedral sites, resulting in a general formula of $B_{\text{tet.}}(BA)_{\text{oct.}}O_4$. Between the regular and inverse spinels are so-called mixed spinels with the general formula of $(A_{1-x}B_x)_{\text{tet.}}(B_{2-x}A_x)_{\text{oct.}}O_4$, where the degree of inversion (x) is $0 < x < 1$ [78].

Many spinel phases can exhibit a wide range of values for the inversion parameter, and the most stable configuration is often determined by the selection of synthesis parameters such as sintering temperature and/or cooling rate. The value of the inversion parameter may change as a consequence of electron transfer, such as in magnetite (Fe_3O_4) where the disorder is observed to increase with increasing temperature [79], or due to actual changes in cation distribution as in $Mg(Al,Fe)_2O_4$ [80].

2.3. Composition and distribution of cations

Due to the structural flexibility of the perovskite-related phases, control of cation composition through substitution is an important method for both producing new phases and modifying the properties of the already existing ones. Depending on which cation site in the structure, *A* (and *Q* for RP phases) or *B*, is being substituted, the cation substitution in perovskite-related structures is referred to either as *A*-site substitution or *B*-site substitution, respectively. Additionally the substitution can either be isovalent or aliovalent depending on the oxidation state of the substituent in comparison to that of the host cation. This results in a high degree of freedom both in possible cation compositions and oxidation states for the transition metal cation(s) in perovskite-related structures.

While the identity of the transition metal at the *B* site is the deciding factor in determining the functional properties of the perovskite-related oxides, the *A*-site substitution can be employed as an important tool in fine-tuning the functional properties through adjusting the oxidation state(s) of the transition metal cation(s). This is seen for example in the $(Ca_{3-x}La_x)Mn_2O_7$ RP oxide system, where an increase in the La content results in evolution from canted antiferromagnet to a charge-ordered state for $x > 0.4$ [81] and finally to a ferromagnetic state with metallic conductivity in the La-rich end ($1 \leq x \leq 2$) [82]. In contrast, similar substitution with tetravalent Th instead of trivalent La results in a ferromagnetic state and an emergence of a strong tunneling-type MR effect already at a very low substitution level of $x = 0.05$ in $(Ca_{3-x}Th_x)Mn_2O_7$ [83].

Whereas the cations occupying the *A* (and *Q*) site are usually divalent or trivalent, the considerably more flexible coordination and redox chemistry allows wider variation range from II to V for the oxidation state of the *B*-site transition metal [84-87]. The crucial role of the *B*-site substitution can be demonstrated for example in the $n = 2$ RP manganese oxides systems, $(La_{1.2}Sr_{1.8})(Mn_{2-x}M_x)O_7$ (*M* = Fe, Co or Cr) [88,89], $(La_{1.4}Sr_{1.6})(Mn_{2-x}Ti_x)O_7$ [90], $(La_{1.4}Sr_{1.6})(Mn_{2-x}Cu_x)O_7$ [91] and $(La_{1.2}Ca_{1.8})(Mn_{2-x}Ru_x)O_7$ [92-95].

The magnetic properties of the parent $(La,Sr)_3Mn_2O_{7-\delta}$ phase are strongly affected by the double exchange (DE) interaction between the neighboring manganese atoms where the lone e_g electron hops from the trivalent Mn to the empty e_g states in tetravalent Mn, *i.e.* $Mn^{III} + Mn^{IV} \Rightarrow Mn^{IV} + Mn^{III}$. The substitution of manganese with Ti, Fe, Co and Cu in general lowers the Curie temperature (T_C) and suppresses the metal-insulator transition, although the strength of the effect varies depending on the cation substituent. This behavior has been expected to result from the tendency of these substituents to disrupt the DE interaction, localizing the itinerant electron and leading to an increase in resistivity and loss of metallic character [88-91].

However an increase in T_C has been observed when substituting manganese with Cr or Ru over a limited substitution range [88,92-95]. In case of Cr this has been attributed to the fact that Cr^{III} exhibits the same electronic structure as Mn^{IV}, whereas the Ru^{IV}/Ru^{V} and Mn^{III}/Mn^{IV} pairs share the similar electron configuration in their outer 4d/3d orbitals, respectively. It has therefore been postulated that the Cr and Ru could participate in DE thus preserving the T_C. However it has been pointed out that although limited Ru (and Cr) substitution increases the T_C it also simultaneously decreases the saturation magnetization and increases the resistivity, which should not occur if these transition metals participated in DE. Due to these reasons it has been suggested that the increase in T_C results from the disorder-induced suppression of charge-orbital order, instead [95].

A strong impact of cation substitution on magnetotransport properties is also encountered in spinel oxides [**VI**], although they exhibit less variety in terms of cation composition and transition metal oxidation state(s) due to being in general highly resistant to changes in oxygen stoichiometry [96,**III**]. On the other hand, the magnetic

properties of the spinel oxides are often more susceptible on the level of magnetic dilution and distribution of magnetic cations in the structure due to the presence of multiple, inherently frustrated magnetic interactions in the spinel structure.

The magnetic properties of the spinel oxides, AB_2O_4, are governed by an intricate interplay between the intrasite *A*-O-*A* and *B*-O-*B* (J_{AA} and J_{BB} respectively) and intersite *A*-O-*B* (J_{AB}) superexchange interactions. It should be noted here that all the exchange interactions are negative, resulting in antiferromagnetic contribution from the intrasite J_{AA} and J_{BB} interactions. On the other hand, although the intersite exchange interaction, J_{AB}, is also negative, the contribution is often ferrimagnetic as there are two *B* sites for each *A* site in the structure and consequently the magnetic moments do not usually cancel out. The presence of multiple competing interactions results in strong frustration in magnetic order and the resulting magnetic properties are strongly dependent on the level of magnetic dilution and distribution of magnetic cations as seen in Figure 3 [97,98].

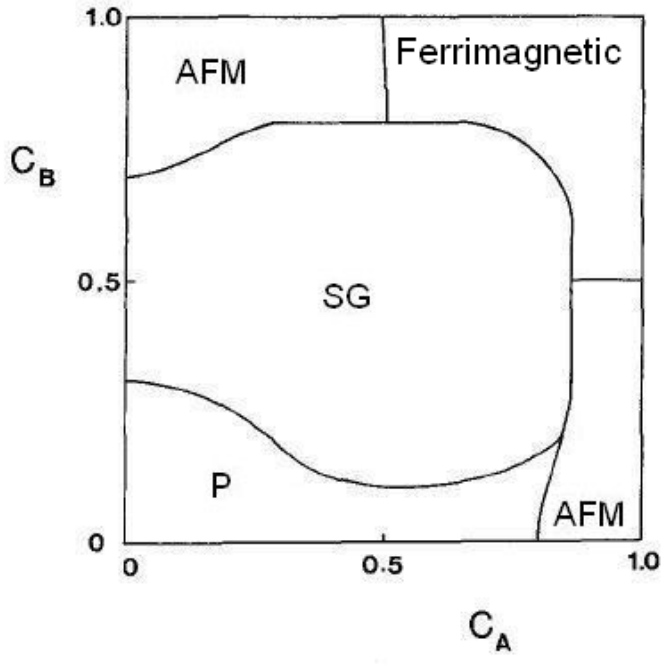

Figure 3: Magnetic phase diagram for the general spinel structure, AB_2O_4, showing paramagnetic (P), antiferromagnetic (AFM), ferrimagnetic and spin glass (SG) regions as a function of the magnetic cation concentrations for the *A* and *B* sites, C_A and C_B, respectively [98].

When both the *A* and *B* sites of the spinel structure are fully occupied by magnetic cations, $J_{AB} >> J_{BB} >> J_{AA}$, and the system usually exhibits a co-linear ferrimagnetic structure due to the strong J_{AB} superexchange interaction [97]. Progress in magnetic dilution then results in weakening of J_{AA}, leading to frustration and formation of non co-linear spin structures (spin canting) or the spin-glass state [99-102, **VI**]. In addition, the magnetic properties of the magnetically diluted spinel phases are sensitive to the distribution of magnetic cations between the *A* and *B* sites, as the confinement of magnetic cations at one site only leads to formation of antiferromagnetic order. Finally, at extreme levels of magnetic dilution, percolation occurs and a paramagnetic state is formed [97,98].

The effect of cation distribution is clearly demonstrated in the $ZnFe_2O_4$ system which can be realized both in regular and mixed-spinel configurations depending on the preparation method. In the regular spinel configuration diamagnetic Zn cations are located at the *A* site and magnetic Fe cations at the *B* site and the magnetic properties of the phase are dominated by the J_{BB} superexchange interaction, resulting in an antiferromagnetic order with $T_N \approx 10$ K [103]. On the other hand, $ZnFe_2O_4$ can also be realized in a mixed-spinel configuration with high magnetization near room temperature [104-106]. The ferrimagnetic order in these samples has been attributed to the emergence of strong ferrimagnetic J_{AB} interaction due to the presence of Fe at both the *A* and *B* sites.

2.4. Determination of cation composition and distribution

2.4.1. ICP-OES

The most common way of synthesizing layered TMOs is the so-called solid-state synthesis method in which the precursor oxides or carbonates are fired at high temperatures to obtain the desired phase. Depending on the identity of cations, the required sintering temperatures can be in the range where the diffusion or evaporation of cations from the precursor mixture can become an issue [107-109]. Therefore it is often necessary to confirm the precise cation composition of the resultant samples.

In the ICP-OES (Inductively Coupled Plasma – Optical Emission Spectroscopy) method plasma is produced by heating up a gas such as argon with electric currents induced by a variable magnetic field. The sample is dissolved and fed into plasma where it dissociates into constituent atoms/ions. The atoms/ions are excited by the high temperature (6 000 – 10 000 K) of the plasma and the relaxation of the excited state produces radiation at characteristic frequency, allowing the identification of the cations based on the wavelengths present in the emission spectra [110].

The intensity of the emission radiation is directly proportional to the number of emitting atoms in plasma and the exact cation composition of each cation can be accurately determined based on a calibration performed with a series of standard samples. The sensitivity of the method is highly dependent on the identity of measured cations, ranging approximately from 0.1 to 100 ppb (1-10 ppb for most transition metal cations) [110,111]. With careful preparation of standard samples and several parallel measurements, the cation composition of the measured sample can be determined with approximately 0.5-1% standard deviation.

However, it should be noted here that if the analyzed sample contains unwanted secondary phases, the cation composition obtained with ICP-OES method will be the (weighed) average of all phases. Therefore it is essential to first confirm the phase purity of the analyzed samples with suitable method such as XRD measurement. In this thesis ICP-OES measurements were used in determining the exact cation stoichiometry of the InFeMO$_4$ oxides, where M = Mg, Co, Ni, Cu and Zn [**V**].

2.4.2. Rietveld refinement

The long heat treatment periods at high temperatures often employed in the solid-state synthesis method may lead to changes in overall cation composition and formation of unwanted impurity phases and/or changes in the cation stoichiometry of the main phase. X-ray diffraction (XRD) measurement is a common method employed to verify the phase purity of layered TMOs. In addition, the structural parameters and cation distribution in the samples can be determined from the XRD data through the Rietveld refinement method [112].

In the Rietveld method [113], the calculated XRD pattern derived from the structural model of the studied phase is compared with the measured diffraction pattern, point by point. During the fitting process, selected parameters of the structural model are adjusted based on the least-squares method to give the best possible fit. These parameters contain instrument-related factors, such as profile function, zero position and background function, in addition to the sample-related variables, such as space group, lattice parameters, atomic positions, occupancies, thermal parameters and preferred orientation. The fitted parameters also include the peak shape parameters, which allow the flexible variation of the selected peak shape function. In this thesis, XRD measurements were employed in determining the phase purity, structural parameters and cation distribution for all the synthesized samples [**II**-**V**].

2.4.3. ^{57}Fe Mössbauer spectroscopy

In the case of iron oxides, ^{57}Fe Mössbauer spectroscopy provides a powerful tool for investigating the changes in distribution, oxidation state, magnetic order and local surroundings of iron atoms at different structural sites [114,115]. These changes produce shifts and splits in the energy levels of the iron nucleus which can be detected for example by employing the resonance absorption phenomenon. However, the changes in the observed energy levels of the iron nucleus are extremely small and the energy losses associated with the emission and absorption of the radiation usually prevent the occurrence of the resonance absorption phenomenon. The Mössbauer spectroscopy is based on the discovery that in certain situations the γ-quantum can be emitted and absorbed without recoil by an atom embedded in a solid matrix, if the energy of the γ-quantum is sufficiently small. The recoilless emission/absorption can occur if the recoil energy is not large enough to be transmitted as a lattice phonon, the whole system recoils and as a result the recoil energy is practically zero.

In recoilless resonance absorption the energy distribution equals the natural line width of the excited nuclear state, as the ground state has infinite lifetime and hence zero uncertainty in energy. If the excited state of the source has the mean life of τ, the energy spread of emitted γ-quantum has the width Γ_s at half height given as

$$\Gamma_s = \frac{\hbar}{\tau} \tag{1}$$

As an example, for the most common Mössbauer isotope, ^{57}Fe, the natural line width is 4.67×10^{-9} eV, whereas the energy of emitted γ-quantum is 14.4 keV, resulting in energy resolution in order of 10^{12} [114,115]. This exceptional resolution allows the observation of hyperfine interactions resulting from the changes in chemical composition, local structure and electric/magnetic fields at the nucleus. Due to the extremely narrow line width, the resonance absorption occurs only when the energy of the γ-quantum emitted from the source exactly matches the transition energy in the absorbing atom (see Figure 4). Therefore the method is isotope specific in nature.

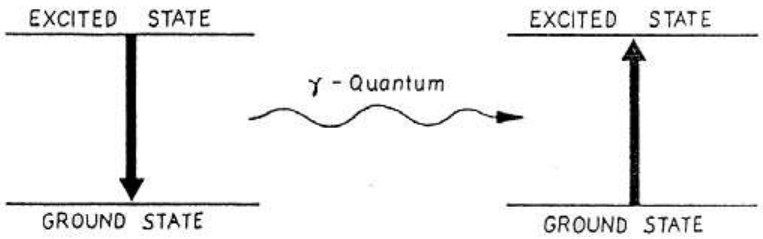

Figure 4: Schematic representation of recoilless emission/absorption of γ-ray photon (Mössbauer spectroscopy) [114].

However, all elements are not suitable for Mössbauer measurements, as the relative strength of the resonance absorption phenomenon and the resolution are dependent on the energy of the γ-quantum and the lifetime of the excited state, respectively [114,115]. Although the Mössbauer effect has been observed for many transition metals and most of the lanthanoids and actinoids (see Figure 5), a vast majority of the research has been performed with iron (so-called ^{57}Fe Mössbauer spectroscopy) due to the limiting factors mentioned above.

1	2	3	4	5	6	7	8	9	10	11	12	13	14	15	16	17	18
1 H																	2 He
3 Li	4 Be											5 B	6 C	7 N	8 O	9 F	10 Ne
11 Na	12 Mg											13 Al	14 Si	15 P	16 S	17 Cl	18 Ar
19 K	20 Ca	21 Sc	22 Ti	23 V	24 Cr	25 Mn	26 Fe	27 Co	28 Ni	29 Cu	30 Zn	31 Ga	32 Ge	33 As	34 Se	35 Br	36 Kr
37 Rb	38 Sr	39 Y	40 Zr	41 Nb	42 Mo	43 Tc	44 Ru	45 Rh	46 Pd	47 Ag	48 Cd	49 In	50 Sn	51 Sb	52 Te	53 I	54 Xe
55 Cs	56 Ba	57 La *	72 Hf	73 Ta	74 W	75 Re	76 Os	77 Ir	78 Pf	79 Au	80 Hg	81 Tl	82 Pb	83 Bi	84 Po	85 At	86 Rn
87 Fr	88 Ra	89 Ac **	104 Rf	105 Db	106 Sg	107 Bh	108 Hs	109 Mt	110 Ds	111 Rg							

58 Ce	59 Pr	60 Nd	61 Pm	62 Sm	63 Eu	64 Gd	65 Tb	66 Dy	67 Ho	68 Er	69 Tm	70 Yb	71 Lu
90 Th	91 Pa	92 U	93 Np	94 Pu	95 Am	96 Cm	97 Bk	98 Cf	99 Es	100 Fm	101 Md	102 No	103 Lr

Figure 5: Periodic table of the elements. Mössbauer active elements are shaded gray. Figure drawn according to data from references [114,115].

The ^{57}Fe Mössbauer spectroscopy is based on the emission of a γ-quantum by a ^{57}Fe nucleus produced in radioactive ^{57}Co source. The emitted γ-quantum is then absorbed by the ^{57}Fe nucleus in the sample. As the environment of ^{57}Fe nucleus has an effect on the transition energy both in the source and the sample, direct transition is only possible if the ^{57}Fe nuclei in the source and target have identical local coordination. This is not, however usually the case. Instead, the different matrix in the sample compared to the source results in a small relative shift in transition energy. The transition energy is also affected by the changes in the s electron density at the nucleus. Due to this, the transition energy is also sensitive to the oxidation state of the host Fe cation. The combined effect on the transition energy is called *Isomer Shift* (*IS*) and the value of the *IS* therefore provides information about the oxidation state of the iron and the local coordination as well. It should be noted here that the value of IS cannot be directly determined, therefore it is given relative to a know reference absorber, such as α-Fe, instead [114,115].

To observe the resonance absorption the energy of the emitted γ-quantum has to be modulated (see Figure 6) to compensate this difference. The necessary modulation of the γ-quantum energy of is usually produced by moving the source producing the γ-quanta. When source moves toward the target the energy of the released γ-quantum is increased due to the Doppler effect. Conversely, when source is moving away from the sample the energy is decreased. Absorption of the γ-quantum is observed when the (modulated) energy of γ-quantum corresponds to the transition energy in the sample [114,115].

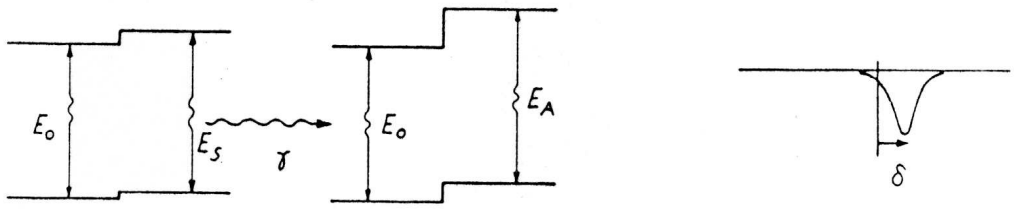

Figure 6: Isomer shift in Mössbauer spectroscopy and its effect on Mössbauer spectra [114].

The transition energy can also be affected by the presence of the electric and/or magnetic fields at the nucleus, due to electric quadrupole interaction and magnetic hyperfine interaction (Zeeman splitting), respectively (see Figure 7). The strength of quadrupole interaction produces information on the order of the charges around the ^{57}Fe nucleus, whereas the magnetic hyperfine interaction provides information about the magnetic order in the sample [114,115].

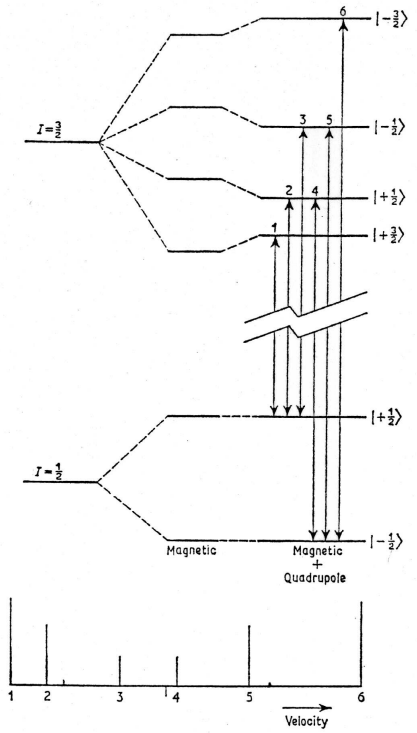

Figure 7: The effect of simultaneous quadrupole splitting and magnetic hyperfine interaction on Mössbauer spectra [114].

For this thesis, a novel fitting model was developed for the fitting of paramagnetic ^{57}Fe Mössbauer spectra of the InFeMO$_4$ system, where M = Mg, Co, Ni, Cu and Zn [**V**], based on a point charge model. The new model was then employed in studying the cation distribution, oxidation state of Fe and the magnetic order in the aforementioned phases in conjunction with Rietveld refinement of XRD data and AC/DC magnetization measurements [**V**,**VI**].

3. OXYGEN CONTENT CONTROL

Besides the cation substitution discussed in the previous chapter, control over the oxygen content of the sample provides us with another important tool to fine-tune the oxidation states of transition metals and thereby the desired functional properties of the layered TMOs. In this chapter the role of the precise oxygen content in RP oxides is discussed, followed by a short summary of the methods employed in controlling and determining the exact oxygen content in the studied samples.

3.1. Oxygen stoichiometry in Ruddlesden-Popper oxides

RP oxides, $A_2Q_{n-1}B_nO_{3n+1-\delta}$, are highly flexible in terms of oxygen content and may contain high concentrations of oxygen vacancies, especially in the *Q*O layer(s), which can be either completely oxygen vacant, or partially or completely filled with oxygen. In cases where *A* and *Q* sites are occupied by trivalent cations, the RP oxides can also accommodate excess oxygen such as observed for example for $La_2NiO_{4+\delta}$ [116] and $La_4Co_3O_{10+\delta}$ [117].

The oxygen-vacancy concentration of RP oxides is seldom presented on layer-by-layer basis; an overall oxygen-nonstoichiometry parameter of δ is usually given instead. The variation range for δ is strongly influenced by the identity of the transition metal. In the case where the transition metal is Cu, the *Q*O layers between the CuO_2 layers are usually fully oxygen depleted, *i.e.* only the bare *Q* cation layers are formed [118-121], whereas for other transition metals such as Fe, Co, Mn and Ni the oxygen content in the *Q*O layers typically varies between 0 (bare *Q* layers) and 1 (full oxygen occupation), depending on the identity of the transition metal in question [122,123,**I-IV]**. An illustrative example is found in the $Sr_3(Fe_{2-x}Co_x)O_{7-\delta}$ system, where the substitution of Fe by Co is accompanied by an increase in the oxygen content, both for as-synthesized [29] and O_2-annealed [29,124] samples. This behavior has been attributed to the relative stability of Fe^{IV} compared to Co^{IV} [29].

The oxygen-vacancy concentration also has a large effect on the coordination number of the transition metal cation in the BO_2 layer(s). The oxygen-stoichiometric configuration in the QO layer results in octahedral coordination, whereas the fully oxygen-vacant configuration results in pyramidal or planar coordination depending on the number of BO_2 layers, n as seen in Figure 8. In the case of partial oxygen occupation in the QO layers, all the above-mentioned coordinations are possible. It has also been reported that the BO_2 layers themselves could possess oxygen vacancies when the QO layers are nearly oxygen depleted [125].

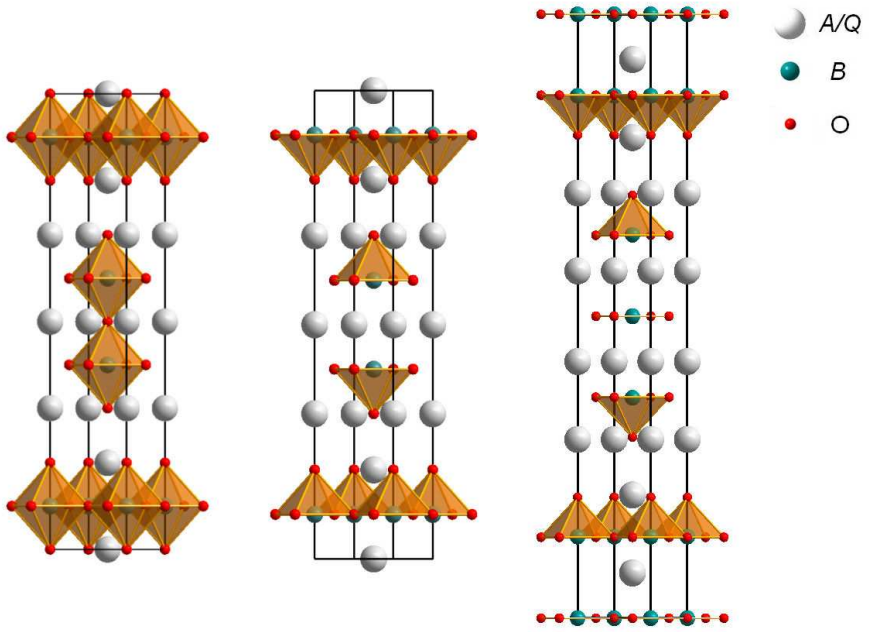

Figure 8: Effect of oxygen vacancy concentration in RP oxides. From left to right, oxygen stoichiometric n = 2 phase, oxygen depleted n = 2 phase and oxygen depleted n = 3 phase. Figure drawn based on the data from Bilbao crystallographic server and reference [36].

Changes in oxygen content directly affect the average transition metal oxidation state. The effect is similar to that resulting from aliovalent cation substitution, although the transition metal valence can often be controlled over a wider range by changing the oxygen vacancy concentration. The effect of oxygen vacancy concentration on the properties is seen for example in the $Sr_3(Fe,Co)O_{7-\delta}$ system, where the oxygen-deficient samples with $\delta \geq 1.1$ exhibit antiferromagnetic (AFM) order, whereas the nearly oxygen-stoichiometric configuration produces a ferromagnetically (FM) ordered state

exhibiting a CMR effect (-24%) at $\delta = 0.1$ [85]. A similar transition from long-range AFM order in oxygen-depleted samples to competition between AFM and FM in oxygenated samples has also been observed for the $Sr_2(Y,Ca)Co_2O_{7-\delta}$ system [66,**II**]. In both cases the AFM order is prevalent in the oxygen-depleted samples which exhibit bare *Q* layers, whereas the introduction of oxygen into the *Q* layers leads to formation of ferromagnetic interaction between the adjacent BO_2 layers.

3.2. Oxygen content determination by chemical methods

Rietveld refinement of the XRD data can be used to roughly establish the oxygen content of the layered TMOs based on the values obtained for the oxygen occupancy at different structural sites. However, the sensitivity of XRD for oxygen is low and the obtained occupancy values are seldom precise, resulting in large errors in the resultant oxygen content values. More precise results can be obtained by employing either synchrotron X-ray or neutron sources, but these methods are expensive and available measurement time is limited.

Therefore methods such as thermogravimetric (TG) measurements and wet-chemical redox titrations are the most convenient and readily available for determining the exact oxygen content in layered TMOs [126-129]. However, as these methods can provide only average oxygen content of the phase, they work best when used in conjunction with site-specific methods such as Rietveld refinement. With the combination of chemical and site-specific methods, it becomes possible to precisely determine the oxygen vacancy concentration and oxidation state of transition metal cations on each structural sub-unit.

3.2.1. Wet-chemical titrations

Among the chemical methods, the redox titrations provide the highest accuracy (typically $\Delta\delta = \pm 0.01$ if a phase-pure sample is analyzed with a number of parallel determinations). For a redox titration the sample is dissolved in an acidic solution and the high-valent transition metal species in the sample are reduced with an excess amount of reductant present in the titration solution. The average transition metal

oxidation state is then calculated based on the amount of excess reductant, determined with a suitable titrant or by forcing a redox reaction with potential difference. The end point can be detected either visually by using an indicator, or measuring the change in the potential difference in the solution with an appropriate indicator electrode in the case of electrochemical redox reaction. Iodometric, cerimetric and coulometric titrations are the wet-chemical methods most often used for the analysis of transition metal oxidation states in transition metal oxides [129]. The choice of method is based on the identity of the transition metal constituent(s) in the sample, as all methods are not suitable for all transition metal elements (see Table 2).

Table 2: Applicability of wet-chemical redox methods for the oxides of high-valent Co, Cu and Fe [**I**].

	Iodometric titration	Cerimetric titration	Coulometric Cu^{+}-titration	Coulometric Fe^{2+}-titration
Applicability in terms of transition metal	Co, Cu	Co, Fe	Co, Cu, Fe	Co, Fe

Cerimetric titration is based on the reduction of high-valent transition metal cations with an excess of Fe^{2+} ions in acidic solution. The remaining divalent iron is titrated with a solution containing tetravalent cerium and the endpoint of the titration is detected with an indicator. The titration solution is standardized with an appropriate standard, such as As_2O_3 or Mohr's salt. In the case of strongly reduced samples, such as those with iron at the mixed $Fe^{II/III}$ oxidation state, a direct cerimetric titration can be performed, where all the Fe^{2+} ions present in the solution are solely from the sample. Cerimetric titration is commonly performed in a closed titration cell under inert atmosphere, such as N_2 or Ar, to prevent oxidation of the reducing agent. The method can be employed for the oxides of Fe and Co, whereas Cu-based samples cannot be analyzed by the technique. In this study the cerimetric titration was used for determining the oxygen content of the $Sr_2(Y,Ca)Co_2O_{7-\delta}$ and $Sr_3Fe_2O_{7-\delta}$ samples [**I-IV**].

Coulometric titration is based on the reduction of high-valent transition metal cations with known excess of either Cu^{+} (Cu^{+}/Cu^{2+} titration) or Fe^{2+} (Fe^{2+}/Fe^{3+} titration) in an acidic solution. The method is more versatile than the cerimetric titration as it can be

used in determining the oxygen content in Fe-, Co- and Cu-based oxides [129,**I**,**II**]. In coulometric titration the excess reductant is oxidized by a constant current in a titration cell (see Figure 9), and the end point of titration is detected with a voltage meter. The oxygen content is calculated based on the amount of the excess reductant, determined from the titration time and current based on Faraday's law. In this study, coulometric titration was used together with the cerimetric titration to confirm the oxygen content in the $Sr_2(Y_{1-x}Ca_x)Co_2O_{7-\delta}$ samples [**I**,**II**].

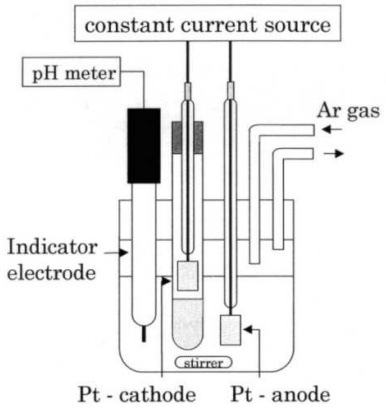

Figure 9: Titration cell for coulometric titration [126].

3.2.2. Thermogravimetry

Thermogravimetric reduction is often used in determining the absolute oxygen content in the TMOs, especially in cases where the sample is difficult or impossible to dissolve. The method is based on the reduction of a sample to known pure metallic/oxide components at elevated temperatures using hydrogen as a reductant, therefore the technique is often called hydrogen reduction. The changes in sample mass can be observed as a function of temperature, allowing the identification of possible intermediate phases in addition to the final residue as seen in Figure 10. The oxygen content can be calculated from the weight difference between the original sample and the residue, although the results are considerably less accurate than those obtained from wet-chemical titrations [16,127,129,**II**]. In this study, hydrogen reduction was used to confirm the oxygen content values obtained from the cerimetric and the coulometric titrations for the $Sr_2(Y,Ca)Co_2O_{7-\delta}$ samples [**I**,**II**].

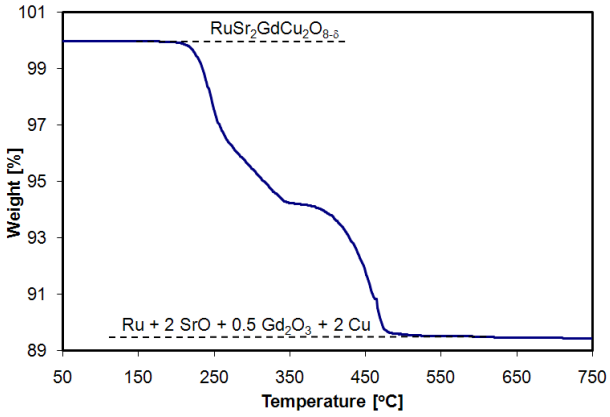

Figure 10: Thermogravimetric H_2 reduction of $RuSr_2GdCu_2O_{8-\delta}$ [16].

Thermogravimetric measurements are also used to follow the changes in the sample´s oxygen content upon oxygenation/deoxygenation treatments [**I-III**]. In addition, TG measurements can be employed in preparing (a series of) samples with fixed, intermediate oxygen-content values by recording a TG curve in a reducing atmosphere for fully oxygenated sample and reading the proper annealing temperatures corresponding to the desired oxygen content from the obtained TG curve as seen in Figure 11.

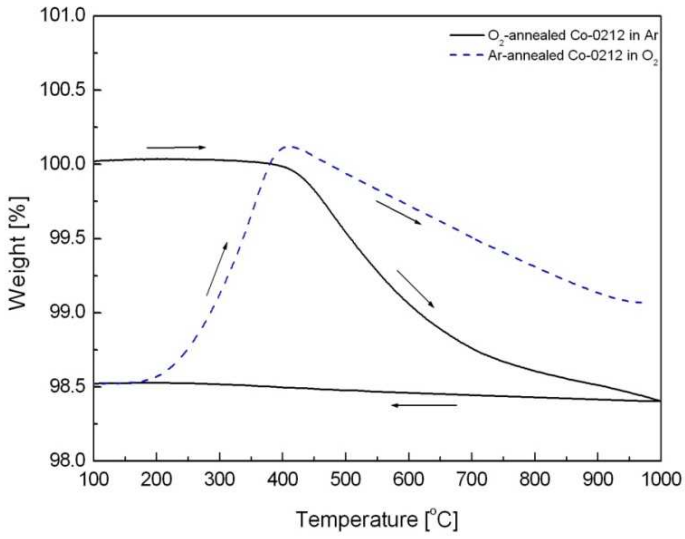

Figure 11: TG curves for the deoxygenation of 1 bar O_2-annealed $Sr_2(Y_{0.5}Ca_{0.5})Co_2O_{7-\delta}$ (Co-0212) sample upon heating and cooling in Ar (solid line), and subsequent oxygenation of the same sample upon heating in O_2 (broken line) [**II**].

4. $Sr_2QCo_2O_{7-\delta}$ RUDDLESDEN-POPPER OXIDES

In the $Sr_2QCo_2O_{7-\delta}$ RP system where Q = Y, Ca and Sr the structural and magnetotransport properties are highly sensitive both to the precise cation composition and the precise oxygen content. Hence they are good candidates for studying the relations between the cation and oxygen stoichiometry and the resultant physical properties.

4.1. Structure and oxygen nonstoichiometry

The parent compound of the $Sr_2QCo_2O_{7-\delta}$ system where Q = Sr, *i.e.* $Sr_3Co_2O_{7-\delta}$, exhibits complex structural and magnetic transitions closely linked to the level of oxygen nonstoichiometry and the ordering of oxygen vacancies. The phase was first reported to possess an ideal RP (tetragonal) structure when $\delta = 0.94$ (oxygen content = 6.06) [130], corresponding to average Co oxidation state of 3.06. In this structure the oxygen vacancies are located in the QO layer between the CoO_2 layers, and Co exhibits a mixture of pyramidal and octahedral coordinations and is shifted slightly from the ideal position at the basal plane of the pyramid/center of the octahedron towards the apical oxygen located in the AO layer. At low oxygen contents a reversible phase transformation has been observed at $\delta > 1$ (oxidation state of Co < 3) to orthorhombic *Immm* space group [84,125,130].

Transition to orthorhombic structure has also been reported for highly oxidized $Sr_3Co_2O_{6.6}$ (oxidation state of Co = 3.6) samples [125]. These samples exhibit an ideal RP structure only at elevated temperatures, whereas orthorhombic strain resulting from buckling of the CoO_2 layers appears at lower temperatures. Due to this, the stable structure at room temperature is orthorhombic (space group *Immm*). The crystal structure of $Sr_3Co_2O_{7-\delta}$ is therefore highly sensitive to the degree and ordering of oxygen vacancies, leading to the limited stability range, both in terms of oxygen content and temperature, for the ideal RP structure.

The oxygen vacancy concentration also has a strong impact on the structural stability of the $Sr_3Co_2O_{7-\delta}$ phases, as the oxidized samples where $\delta < 1$ (oxidation state of Co > 3) have been found to be highly sensitive to ambient humidity [65,125]. This is expected to result from the presence of highly unstable tetravalent Co and due to this the oxidized $Sr_3Co_2O_{7-\delta}$ phases exhibit a strong tendency for reduction of Co and inherent structural instability, similar to that observed for the related $Sr_3Fe_2O_{7-\delta}$ system [**III**,**IV**] discussed in more detail in the next chapter.

If the high oxidation state of Co is the main contributing factor for the instability, more stable phases should be obtained through aliovalent *A*-site substitution of divalent strontium with trivalent cation, as the average oxidation state of Co would decrease with increasing trivalent substitution. This effect has indeed been observed by substituting the Sr in the *Q*O layer with Ca and a wide range of (trivalent) rare earth elements (*RE*) in $Sr_2(RE,Ca)Co_2O_{7-\delta}$ system [66,**II**]. These phases, unlike the parent $Sr_3Co_2O_{7-\delta}$ system, are not sensitive to ambient humidity even when highly oxidized. In addition, the substitution stabilizes the ideal RP structure, as the oxygen stoichiometry-driven transition to the orthorhombic *Immm* space group has not been observed.

The degree of aliovalent substitution has also a strong effect on the variation range of the oxygen vacancy concentration as demonstrated in the $Sr_2(Y_{1-x}Ca_x)Co_2O_{7-\delta}$ system [**II**]. It was observed that the lower limit for oxygen content remains nearly constant (*i.e.* $\delta \approx -1.2$) for $0.3 \leq x \leq 0.5$ [**II**], whereas the maximum oxygen content was seen to significantly increase with increasing trivalent substitution from $\delta = -0.77$ for $x = 0.5$ to $\delta = -0.52$ for $x = 0.3$ for the fully oxygenated samples (see Figure 12). The increase in maximum oxygen content is expected to be due to the decrease in Co oxidation state with increasing trivalent substitution. The range for stable oxygen contents can also be further expanded by external stabilization of the high oxidation states for Co as reported for the $Sr_2(Y_{0.5}Ca_{0.5})Co_2O_7$ phase, where the oxygen stoichiometric composition was obtained through high-pressure treatment [131].

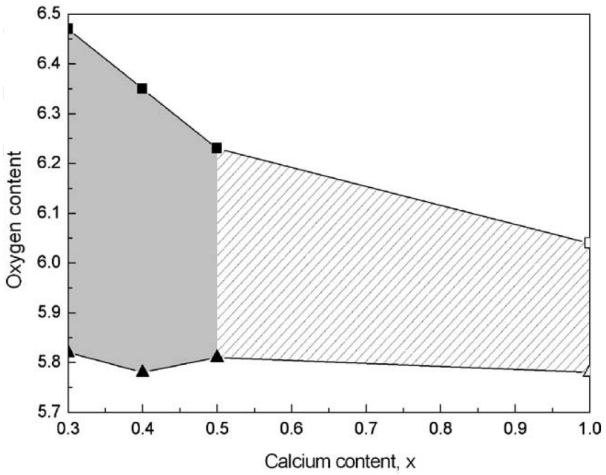

Figure 12: Minimum (filled triangles; Ar-annealed samples) and maximum (filled squares; O_2-annealed samples) oxygen contents for the $Sr_2(Y_{1-x}Ca_x)Co_2O_{7-\delta}$ samples. The data for the $Sr_3Co_2O_{7-\delta}$ sample (open triangles for the minimum, open squares for the maximum oxygen content) are from Ref. [130], and plotted in the figure as a reference case [**II**].

4.2. Magnetotransport properties

Oxygen stoichiometry/oxidation state of cobalt has a strong impact on the magnetotransport properties of the $Sr_2(Y_{1-x}Ca_x)Co_2O_{7-\delta}$ phases as well. Oxygen depleted $Sr_2(Y_{1-x}Ca_x)Co_2O_{7-\delta}$ samples are insulating and exhibit long-range AFM order, whereas oxygenated samples exhibit FM order and lower resistivity (several orders of magnitude) [66,131,**II**] as seen in Figure 13. The conduction in (nearly) oxygen-stoichiometric $Sr_2(Y_{0.5}Ca_{0.5})Co_2O_{7-\delta}$ at low temperatures has been explained by Efros-Shklovskii-type variable range hopping, whereas with increasing temperature there is a crossover to Mott-type variable range hopping [131]. A weak MR effect is observed in the oxygenated $Sr_2(Y_{1-x}Ca_x)Co_2O_{7-\delta}$ samples [**II**].

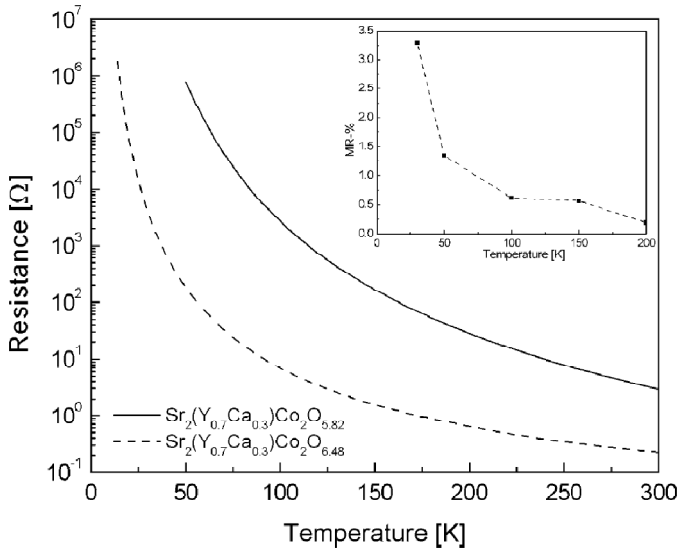

Figure 13: Resistance vs temperature for oxygen-depleted (solid line) and oxygenated (broken line) $Sr_2(Y_{0.7}Ca_{0.3})Co_2O_{7-\delta}$ samples. Inset shows the MR behavior for the oxygenated sample [**II**].

The crossover from AFM order in oxygen-depleted $Sr_2(Y_{1-x}Ca_x)Co_2O_{7-\delta}$ samples to FM order in oxygenated samples is related to the amount of oxygen in the (Y,Ca)O layer between the neighboring CoO_2 layers. The oxygen atoms in the (Y,Ca)O layer facilitate the formation of FM bonds, resulting in competition between the AFM and FM interactions at low temperatures [66,**II**]. This competition introduces the element of frustration into the system, which, combined with the inherent randomness derived from the presence of oxygen vacancies and random distribution of Y and Ca, facilitates the formation of a glassy state. This is evident in the divergence of FC and ZFC curves in the M-T magnetization measurements and the time-dependent nature of the magnetization. Due to the saturating behavior of the FC curve above the divergence point it is reasonable to expect the fully oxygenated $Sr_2(Y_{1-x}Ca_x)Co_2O_{7-\delta}$ samples to form a conventional spin-glass state instead of a cluster glass or a superparamagnet, as in these cases the FC curve would be expected to increase monotonically with decreasing temperature. However, AC-magnetization measurements would be necessary to probe the exact nature of the glassy state in $Sr_2(Y_{1-x}Ca_x)Co_2O_{7-\delta}$.

5. WATER DERIVATIVES OF *n* = 1-3 RP OXIDES

The rock-salt-structured $(AO)_2$ double layer between two adjacent perovskite blocks in $A_2Q_{n-1}B_nO_{3n+1-\delta}$ RP oxides can easily accommodate additional structural elements and consequently these oxides can form *e.g.* topotactic water derivative phases when subjected to ambient humidity, as seen in Figure 14. For example the n = 1 RP phases $Ba_2ZrO_{4-\delta}$ [33] and (Na,Eu)$TiO_{4-\delta}$ [34] and the n = 3 RP phases, $Sr_2(Sr,La)Fe_3O_{10-\delta}$ [57], $Sr_4(Co_{1.6}Ti_{1.4})O_{10-\delta}$ [132] and $Sr_2(Sr,Nd)Fe_3O_{10-\delta}$ [35] have been observed to form "watery" derivatives. Among these oxides, (Na,Eu)$TiO_{4-\delta}$ forms an exception, as *A*-site ordering has been observed for this phase results in the final layer sequence of NaO-NaO-TiO_2-EuO-EuO-TiO_2, *i.e.* Na and Eu segregate into different layers and do not form mixed (Na,Eu)O layers. During the intercalation process water has been observed to go only between the NaO layers [34].

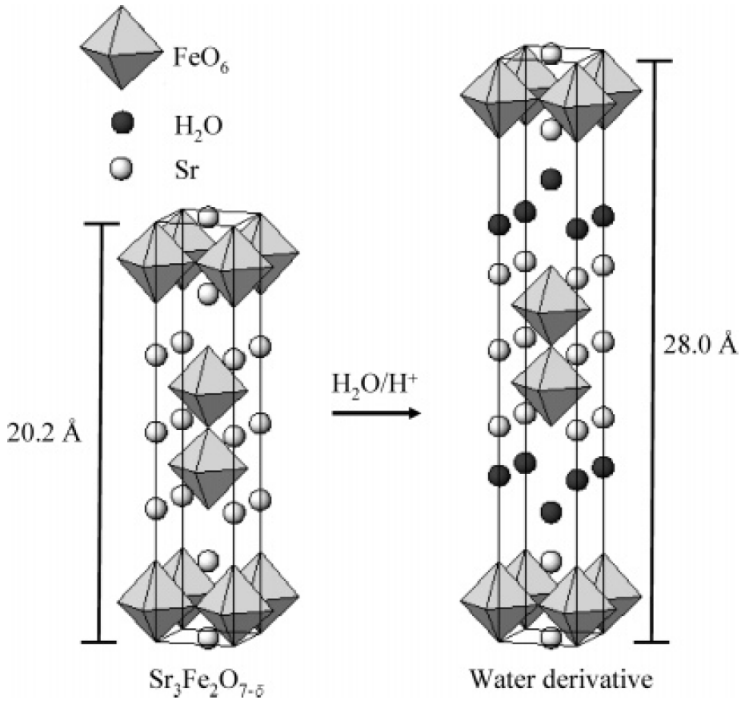

Figure 14: The formation of layered derivative for the n = 2 RP phase, $Sr_3Fe_2O_{7-\delta}$ [**III**,**IV**].

The n = 2 RP phases such as $Sr_3Co_2O_{7-\delta}$ [65], $Sr_3(Co_{0.95}Nb_{0.05})_2O_{7-\delta}$ [133] and $Sr_3(Co_{0.85}Ti_{0.15})_2O_{7-\delta}$ [132] have also been observed to form layered water derivatives. Especially in the case of the $Sr_3Co_2O_{7-\delta}$ phase, the as-synthesized phase is highly unstable and reacts almost immediately to the derivative phase, making the study of the intercalation mechanism difficult in these systems. It is expected that the instability of tetravalent Co is at least partially responsible for the high rate of the intercalation reaction. As the tetravalent oxidation state for iron is more stable, the corresponding Fe-based series, $Sr_{n+1}Fe_nO_{3n+1-\delta}$ (n = 1, 2, 3 and ∞), should be more suited for studying the water intercalation process.

In this thesis, the n = 1-3 members of the $Sr_{n+1}Fe_nO_{3n+1-\delta}$ series were found to absorb water when subjected to varying levels of ambient humidity, with the rate of the reaction increasing with decreasing n [**III**,**IV**]. On the other hand, the n = ∞ member, which is nothing but the $SrFeO_{3-\delta}$ perovskite and lacks the $(SrO)_2$ double layer, did not absorb water even when subjected to extreme levels of humidity (dipped into water) [**IV**]. It could therefore be concluded that the $(AO)_2$ double layer found in RP oxides is necessary for the formation of the layered hydrate derivatives.

The nature of the water-intercalation process was investigated in detail for the n = 2 member of the $Sr_{n+1}Fe_nO_{3n+1-\delta}$ series [**III**]. It was found that the oxidation state of iron is lowered upon the water absorption. This indicates that, in addition to the charge-neutral H_2O molecules, also positively charged H^+/H_3O^+ species are incorporated into the lattice, confirming that the high oxidation state of the transition metal is one of the contributing factors in the destabilization of the ideal RP structure and formation of the intercalated derivative phases. Similar reduction in transition metal valence resulting from the formation of the layered water derivative has also been observed for the $Ba_2Ca_2Cu_3O_8$ [30] and $Sr_3(Co,Nb)_2O_{7-\delta}$ [133] RP oxides, further supporting this conclusion.

Rather interestingly, it was also found that the rate of derivative-phase formation increased with decreasing oxygen content of the parent $Sr_3Co_2O_{7-\delta}$ phase [**III**]. This is counterintuitive, as the decrease in oxygen content lowers the transition metal oxidation state, which should decrease the reaction rate. It is therefore expected that while the

high oxidation state of the transition metal is the thermodynamical driving force for the derivative-phase formation, the reaction rate is enhanced when the concentration of oxygen vacancies is increased. The increase in oxygen-vacancy concentration is expected to provide new pathways for water intercalation, thus facilitating the diffusion reaction and increasing the reaction rate. Correspondingly, it can be postulated that the (nearly) oxygen stoichiometric RP oxides should be more stable in air, as the lack of oxygen vacancies should considerably slow down the intercalation process, although the average transition metal valence increases with the increasing oxygen content of the phase.

The rate of the intercalation reaction was also found to be affected by the level of humidity the sample was exposed to. For all samples the rate of intercalation reaction increased with increasing humidity, although the behavior under extreme humidity differs between the different members of the $Sr_{n+1}Fe_nO_{3n+1-\delta}$ series. The n = 3 member was observed to be relatively stable at ambient humidity and intercalation occurred over a prolonged period of time, whereas the n = 2 member formed the intercalated derivative at a greater rate under similar conditions. The intercalated derivatives were fundamentally unstable and decomposed to $Sr_3Fe_2(OH)_{12}$ [134] of the cubic crystal structure for n = 2 and a mixture of $Sr_3Fe_2(OH)_{12}$ and $Sr(OH)_2 \bullet 8\,H_2O$ for n = 3. The decomposition resulted either from prolonged exposure to ambient humidity or when the derivative was exposed to extreme humidity (saturated water vapor or dipping into water) [**III**,**IV**]. The intercalated derivative of the n = 1 member was more unstable, rapidly decomposing to $Sr(OH)_2 \bullet H_2O$ and $Sr_3Fe_2(OH)_{12}$. Therefore it was nearly impossible to separate the layered derivative in phase-pure form, as it always existed as a mixture either with the original RP phase or the decomposed form [**IV**].

The water intercalation resulted in an increase in the length of the c-axis by ~4.6 and ~4 Å per formula unit for the n = 1 and 2 members, respectively. The value agrees (though being slightly higher) with the values reported for other RP systems [30-32,34,35,57,132]. As discussed above, it was practically impossible to isolate the derivative phase in single-phase form for the n = 1 member, whereas two different derivatives could be observed for the n = 2 member, one with two water molecules per formula unit obtained by exposing the parent RP phase to ambient humidity, and the other one with one water molecule per formula unit obtained by annealing the first

derivative at around 100 ^{o}C. For the n = 3 member, a mixture of various derivatives with different water contents was obtained. The intercalation process is reversible as was seen for both the n = 2 and 3 members, where the parent RP phase could be obtained by removing the intercalated water from the structure with annealing at a suitable temperature [**III**,**IV**]. However, it should be noted that only the formation of the layered derivative is a reversible process, whereas once the intercalated derivative(s) decompose to *e.g.* $Sr_3Fe_2(OH)_{12}$, the parent RP structure can no longer be recovered.

6. SYNTHESIS AND CHARACTERIZATION OF InFe*M*O_4 SPINEL OXIDES (*M* = Mg, Co AND Ni)

In contrast to the perovskite-derived structures, the spinel structure is usually highly resistant to changes in oxygen content [96], although the spinels containing lithium commonly exhibit oxygen nonstoichiometry [135,136]. The presence of oxygen vacancies is usually countered by the formation of cation vacancies rather than change in the average transition metal oxidation state [137]. Instead, the magnetotransport properties in spinel oxides are strongly affected by relatively small changes in cation composition, cation distribution and the level of magnetic dilution, thus offering an interesting subject for studying the underlying dependencies between cation stoichiometry/distribution and the physical properties.

6.1. Formation of InFeMO_4 phases (M = Mg, Co and Ni)

The flexibility of the perovskite structure in terms of cation composition is largely derived from the ability of the oxygen-tunable perovskite phases to compensate for changes in the average transition metal oxidation state, occurring when the precursor cation composition and/or the synthesis conditions (temperature and atmosphere) deviate from the preferred ones. The spinel phases, on the other hand, usually exhibit a (nearly) stoichiometric oxygen content [96], resulting in a much more limited precursor composition-synthesis condition window for phase-pure samples.

In this thesis the high oxygen-stability was confirmed for the InFeMO_4 (*M* = Mg, Co and Ni) phases by means of thermogravimetric annealing experiments. It would therefore be expected that the further aliovalent substitution of trivalent Fe with divalent Mg would result in formation of impurity phases due to resulting changes in the average transition metal oxidation state. On the other hand, Co and Ni exhibit both divalent and trivalent oxidation states and should therefore be able to form a (limited) series of solid solutions, $In(Fe_{1-x}M_{1+x})_2O_4$, as observed for the parent $(Co,Fe)_3O_4$ and $(Ni,Fe)_3O_4$ phases [138,139].

However, attempts to realize such solid solutions resulted in the formation of either impurity phases or the disappearance of the desired phase altogether for $x \neq 0$, as is shown in Figure 15 for M = Ni. The observed behavior is attributed to the tendency of Co and Ni to strongly favor the divalent oxidation state in the present structure, whereas Fe exclusively adopts the trivalent oxidation state [**V**].

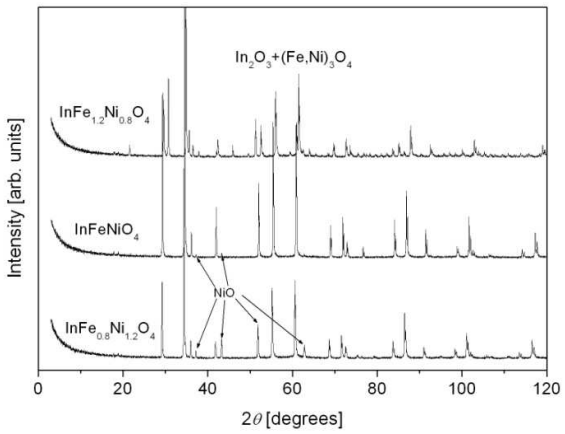

Figure 15: XRD diffraction patterns of the $InFe_{1-x}Ni_{1+x}O_4$ system, where $-0.2 \leq x \leq 0.2$, demonstrating the formation of impurity phases when $x \neq 0$ [**V**].

The $InFeMO_4$ phases (M = Mg, Co and Ni) are also very sensitive to minute changes in cation composition. All phases form as mixed spinels, *i.e.* divalent and trivalent cations co-exist at the A and B sites. The precise cation compositions in the X-ray pure samples were observed to slightly deviate from the nominal chemical composition, $InFeMO_4$, being $In_{1.03}Fe_{0.98}Mg_{0.99}O_4$, $In_{0.985}Fe_{0.952}Co_{1.063}O_4$ and $InFe_{0.98}Ni_{1.02}O_4$; attempts to stabilize the nominal cation compositions (by employing different synthesis temperatures and atmospheric conditions) resulted in formation of impurity phases [**V**]. It should be noted here that for the sake of convenience these phases are later referred by the nominal chemical formulas, $InFeMgO_4$, $InFeCoO_4$ and $InFeNiO_4$ rather than the exact chemical compositions.

6.2. Fitting of Mössbauer spectra of cation-disordered spinel

Mössbauer spectroscopy is a powerful tool for probing the oxidation state and the (local) magnetic order of Mössbauer active atoms in addition to providing information about the identity and ordering of the neighboring cations. Due to the combined effect of different hyperfine interactions (isomer shift, electric and magnetic hyperfine interactions), each nucleus with different oxidation state, magnetic state and/or local surrounding produces a different signal. The resultant Mössbauer spectrum is the sum of all these signals (components), although often the final number of distinguishable components is smaller than the number of different states, as the components produced by two nuclei in similar surroundings overlap strongly.

It is common that the (paramagnetic) Mössbauer spectra of spinel compounds is fitted with a two-component model by assigning one component for the *A* and *B* sites, each [140-143]. However, such model only has a limited capability to describe the disorder often present in spinel compounds. The current $InFeMO_4$ (*M* = Mg, Co and Ni) samples exhibit significant structural disorder due to the presence of all cations at both the *A* and *B* sites, except for the *A* site in $InFeMgO_4$ [**V**]. The effect of this disorder is evident both in the paramagnetic and magnetically ordered spectra of all samples, and consequently the traditional two-component fitting model fails to satisfactorily explain the detailed features in the Mössbauer spectra.

To determine the number of components needed to accurately describe the disorder around both cation sites, a simulation of the paramagnetic Mössbauer spectrum based on a point-charge model was employed. The paramagnetic situation was chosen as a basis for the simulation, as the interaction of ^{57}Fe nucleus with neighboring atoms can be described by calculating the full electric field gradient (EFG) at the Fe nucleus, whereas in a magnetically ordered case a mixed Hamiltonian of combined electric and magnetic interactions is required to adequately describe the situation [**V**].

The simulation is based on determining the strength of electric quadrupole interactions as characterized by the absolute value of the quadrupole coupling constant (*QCC*), extracted from the value of the EFG at the Fe nucleus. In the simulation, a sphere of roughly 7.1 Å in diameter was constructed around both the *A* and *B* sites, and

neighboring cation sites located within the sphere were randomly populated based on the site-specific occupancy values for In, Fe and *M* cations. The probability of the created distribution was calculated and the components of EFG (V_{ij}) were obtained from the common definition [115] of

$$V_{ij} = \sum_k \frac{q_k}{4\pi\varepsilon_o} \frac{1}{r_k^5}(3x_i x_j - \delta_{ij} r_k^2) \tag{2}$$

where k is an index running over all neighboring lattice sites within the sphere, q_k, x_i and x_j are the charge and coordinates of the atoms at the neighboring lattice sites and δ_{ij} is the Kronecker delta.

The resulting matrix is diagonalized and the values of V_{zz} and η can be now extracted. V_{zz} was defined as the largest diagonal term of the matrix and

$$\eta = \frac{|V_{yy}| - |V_{xx}|}{|V_{zz}|} \tag{3}$$

The value of quadrupole coupling constant can now be obtained as

$$QCC = eQV_{zz}(1+\eta^2/3)^{1/2} \tag{4}$$

and converted to units comparable with measured value of *QCC* as described in detail in Ref. **V**.

A large number ($1\text{-}2\times10^6$) of local cation environments were subjected to similar treatment and the simulated *QCC* and probability pairs were gathered and plotted in a histogram. The histograms obtained for the *B* site of the *M* = Mg, Co and Ni phases clearly demonstrate that two individual components with different *QCC* values are required to describe the disorder resulting from the random distribution of In, Fe and *M* cations around the Fe nucleus. An example of such histogram for *M* = Co is shown in Figure 16a. On the other hand, similar histograms for the tetrahedral *A* site for all samples exhibited only a broad distribution as seen in Figure 16b for *M* = Co. It is

expected that the current model cannot fully describe the structural disorder around the tetrahedral site, such as the deviation of oxygen atoms from their ideal positions, resulting in too small variation in the calculated values of EFG and a broad peak for distribution function instead of two distinct components as seen for the octahedral site [**V**].

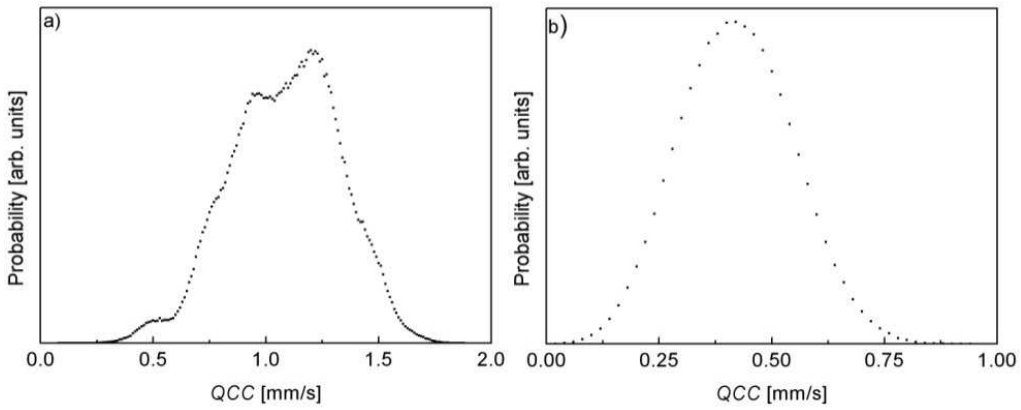

Figure 16: Probability vs. *QCC* histograms for the a) *B* and b) *A* sites of $InFeCoO_4$ [**V**].

The validity of this assumption was tested by fitting the experimental Mössbauer data for the $InFeMO_4$ samples with *M* = Mg, Co and Ni with both the 3-component (one component for tetrahedral, two for octahedral) and the 4-component (two for both sites) models, with the 4-component model producing consistently better fitting results for all samples, whereas the addition of further components did not provide improvement in the quality of the fit [**V**]. The new fitting model was also employed in fitting the magnetically ordered Mössbauer spectra of the $InFeMO_4$ (*M* = Mg, Co and Ni) phases, resulting in good agreement of hyperfine parameters with those obtained from the room-temperature (paramagnetic) spectra and overall increase in quality of the fit compared with the traditional two-component fitting model [**VI**].

It can therefore be concluded that the traditional fitting model is unable to adequately describe the disorder arising from the random arrangement of the cations in the $InFeMO_4$ (*M* = Mg, Co and Ni) spinel phases, whereas the employment of the four-component fitting model significantly increases the quality of the obtained fit. It should also be noted that while the validity of the four-component fitting model was confirmed

only for the InFeMO$_4$ samples with M = Mg, Co and Ni, it is reasonable to expect that similar improvements would be obtained by employing the new model in the fitting of any spinel samples with a similar degree of variation in local environment around the Fe site.

6.3. Effect of cation substitution on magnetotransport properties

Magnetic properties of the spinel phases are governed by an intricate interplay of the intrasite A-O-A and B-O-B (J_{AA} and J_{BB}, respectively) and intersite A-O-B (J_{AB}) superexchange interactions. When both the A and B sites of the spinel structure are fully occupied by magnetic cations, the J_{AB} interaction is dominant, whereas the substitution with nonmagnetic cation(s) can lead to structural disorder and frustration in magnetic order by weakening the J_{AB} superexchange to a level comparable with J_{AA} and J_{BB}. When both of these phenomena occur simultaneously, the structure fulfills the basic criteria generally associated with the emergency of spin-glass type state, namely randomness, presence of magnetic interactions, anisotropy and frustration.

In the InFeMO$_4$ (where M = Mg, Co and Ni) spinel system the necessary randomness is derived from the distribution of In, Fe and M cations over the two structural sites, whereas the presence of the nonmagnetic indium (and Mg) gives rise to frustration in the magnetic order. Therefore it is not unexpected that the InFeMO$_4$ spinel phases of M = Mg and Co were observed to exhibit glassy behavior (see Figure 17). The observed behavior was attributed to the formation of cluster-glass type rather than conventional spin-glass state [**VI**]. Interestingly, although similar behavior would be expected also for the InFeNiO$_4$ phase due to the similar degree of randomness and frustration derived from the cation distribution and magnetic dilution, respectively, the existence of a glassy phase (or reason for the absence of it) could not be decisively confirmed [**VI**].

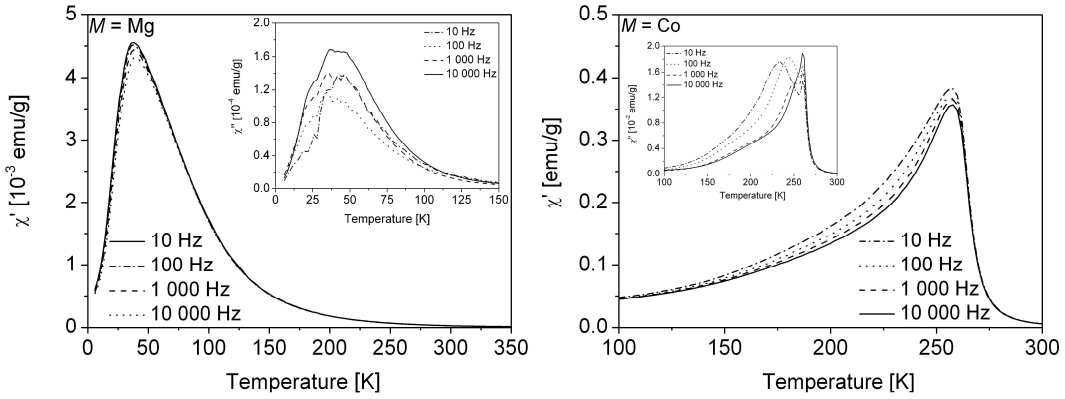

Figure 17: AC magnetization vs. temperature for InFeMO$_4$ spinel oxides, where M = Mg and Co [**VI**].

The magnetic dilution often results in the formation of non-collinear spin arrangement, as well [99]. Such behavior is observed for the $InFeNiO_4$ phase where the observed value of the saturation magnetization (2.1 μ_b/f.u.) is far below the value (3.19 μ_b/f.u.) expected from the Néel's model for collinear ferrimagnet, thus confirming the presence of spin canting [**VI**]. The presence of spin canting is also expected for the M = Mg and Co phases. However, the degree of canting cannot easily be established for these phases, as the presence of cluster-glass state also affects the value of saturation magnetization [**VI**].

Despite the magnetic dilution, both M = Co and Ni phases exhibit a high degree of magnetization near room temperature, as the presence of magnetic cations (Fe and M) at both cation sites facilitates the formation of strong J_{AB} superexchange interaction and the dominance of ferrimagnetic order. The identity of the M cation has, however, a significant effect on the magnetic order, as $InFeCoO_4$ was found to exhibit strong hysteresis at low temperatures whereas the replacement of Co with Ni results in soft magnet-type behavior [**VI**]. In contrast, significantly lower values of magnetization have been observed for $InFeMgO_4$ due to increasing magnetic dilution [**VI**]. However, it has been established that short-range ferrimagnetic order persists [**VI**], although the system is close to the percolation limit [97].

7. CONCLUSIONS

The desired functional properties of layered TMOs are largely dependent not only on the identity but also on the oxidation state and local coordination of the transition metal constituent(s). Therefore control over the cation and oxygen stoichiometry is an effective tool in manipulating the properties of the layered TMOs. In this thesis the effects of cation and oxygen compositions on the structural stability and magnetic and (magneto)transport properties have been studied in selected Ruddlesden-Popper and spinel oxide systems.

In the $Sr_2(Y,Ca)Co_2O_{7-\delta}$ system, the impact of aliovalent *A* site substitution on variation range of oxygen vacancy concentration and the stability of the ideal RP structure were demonstrated. The lower limit for oxygen content remained nearly constant for all samples, whereas the maximum oxygen content was seen to significantly increase with increasing trivalent substitution due to the decrease in Co oxidation state (for the same oxygen content). In addition, the decrease in Co oxidation state stabilized the ideal RP structure, as the substituted samples did not form the layered water derivatives when exposed to (ambient) humidity.

In addition, the impact of oxygen stoichiometry on resistivity and magnetic properties of $Sr_2(Y,Ca)Co_2O_{7-\delta}$ was confirmed. The oxygen-depleted samples exhibited significantly higher resistivity and AFM order, whereas the oxygen in the (Y,Ca)O layer stabilized the ferromagnetic bonds between the adjacent CoO_2 layers and resulted in the formation of a glassy state due to competition between AFM and FM order. In future it would be interesting to study the exact nature of the glassy state further for example with AC magnetization measurements.

The structural instability of the RP oxides was studied in detail in the $Sr_{n+1}Fe_nO_{3n+1-\delta}$ series, where n = 1, 2, 3 and ∞ and the formation of layered water derivatives was first time demonstrated for n = 1, 2 and 3 phases. The high oxidation state of the transition metal was observed to be the main contributing factor for the destabilization of the RP

structure, as the water intercalation is followed by the decrease of the oxidation state of Fe for the n = 2 member. The kinetic constraints were also observed to play an important role, as well, as the intercalation rate was found to increase with increasing oxygen vacancy concentration. The increase in the number of BO_2 layers, n, in the infinite-layer block was observed to stabilize the RP structure and slow down the intercalation reaction. However, it is unclear if this results from the stabilization of the $Sr_{n-1}Fe_nO_{3n-1}$ infinite-layer block with increasing n, changes in oxygen vacancy distribution or the introduction of additional kinetic barriers for water intercalation. Further information on the intercalation process and the exact structure of the intercalation products could be obtained by exposing the $Sr_{n+1}Fe_nO_{3n+1-\delta}$ samples to deuterium-enriched water and performing neutron powder diffraction (NPD) measurements to the thus obtained samples.

The phase formation and impact of the identity of the transition metal and level of magnetic dilution on the magnetic properties were studied in the $InFeMO_4$ system, where M = Mg, Co, Ni, Cu and Zn. The phases exhibiting spinel structure were observed to go through a complex evolution in magnetic properties from ferrimagnet exhibiting large remnant magnetization and glassy behavior for M = Co, to canted soft-magnet structure observed for M = Ni and loss of long-range magnetic order in M = Mg. As variations in the cation distribution and grain size have strong effect on the magnetic properties of spinel phases, it would be interesting to study the functional properties of the $InFeMO_4$ spinel phases grown as thin film samples. Such work is already in progress for the $InFeCoO_4$ phase.

In addition, it was demonstrated that the conventional fitting model often employed in analyzing the Mössbauer spectra of (paramagnetic) cation-disordered spinel phases is not sufficient to adequately describe the local disorder in these phases. Therefore an improved model was developed for the characterization of cation distribution, iron oxidation state and magnetic order in these systems.

REFERENCES

[1] J. G. Bednorz and K. A. Mueller, *Z. Phys. B: Condens. Matter* **64** (1986) 189.

[2] R. von Helmolt, J. Wecker, B. Holzapfel, L. Schultz and K. Samwer, *Phys. Rev. Lett.* **71** (1993) 2331.

[3] R. von Helmolt, K. Samwer, L. Haupt and K. Baerner, *J. Appl. Phys.* **76** (1994) 6925.

[4] S. Jin, T. H. Tiefel, M. McCormack, R. A. Fastnacht, R. Ramesh and L. H. Chen, *Science* **264** (1994) 413.

[5] M. McCormack, S. Jin, T. H. Tiefel, R. M. Fleming, J. M. Phillips and R. Ramesh, *Appl. Phys. Lett.* **64** (1994) 3045.

[6] C. N. R. Rao and B. Raveau, *Colossal Magnetoresistance, Charge Ordering and Other Novel Properties of Manganates and Related Materials*. World Scientific Publishing Company, 1998.

[7] A. P. Ramirez, *J. Phys.: Condens. Matter* **9** (1997) 8171.

[8] A. C. Masset, C. Michel, A. Maignan, M. Hervieu, O. Toulemonde, F. Studer, B. Raveau and J. Hejtmanek, *Phys. Rev. B* **62** (2000) 166.

[9] I. Terasaki, Y. Sasago and K. Uchinokura, *Phys. Rev. B* **56** (1997) R12685.

[10] T. Motohashi, E. Naujalis, R. Ueda, K. Isawa, M. Karppinen and H. Yamauchi, *Appl. Phys. Lett.* **79** (2001) 1480.

[11] S. Hebert, S. Lambert, D. Pelloquin and A. Maignan, *Phys. Rev. B* **64** (2001) 172101/1.

[12] I. Terasaki, *Frontiers Magn. Mater.* (2005) 327.

[13] I. Felner, U. Asaf, Y. Levi and O. Millo, *Phys. Rev. B* **55** (1997) R3374.

[14] C. Bernhard, J. L. Tallon, C. Niedermayer, T. Blasius, A. Golnik, E. Brucher, R. K. Kremer, D. R. Noakes, C. E. Stronach and E. J. Ansaldo, *Phys. Rev. B* **59** (1999) 14099.

[15] V. P. S. Awana, M. Karppinen, H. Yamauchi, M. Matvejeff, R. S. Liu and L. Y. Jang, *J. Low Temp. Phys.* **131** (2003) 1211.

[16] M. Matvejeff, V. P. S. Awana, L. Y. Jang, R. S. Liu, H. Yamauchi and M. Karppinen, *Physica C* **392-396** (2003) 87.

[17] B. Raveau, C. Michel, M. Hervieu and J. Provost, *Physica C* **153-155** (1988) 3.

[18] A. Maignan, C. Martin and B. Raveau, *J. Supercond.* **13** (2000) 313.

[19] Y. Tokura and Y. Tomioka, *J. Magn. Magn. Mater.* **200** (1999) 1.

[20] A. Maignan, C. Martin, D. Pelloquin, N. Nguyen and B. Raveau, *J. Solid State Chem.* **142** (1999) 247.

[21] V. P. S. Awana, J. Nakamura, J. Linden, M. Karppinen and H. Yamauchi, *Solid State Commun.* **119** (2001) 159.

[22] J. Nakamura, J. Linden, M. Karppinen and H. Yamauchi, *Appl. Phys. Lett.* **77** (2000) 1683.

[23] Y. H. Huang, M. Karppinen, H. Yamauchi and J. B. Goodenough, *Phys. Rev. B* **73** (2006) 104408/1.

[24] S. Nakashima, K. Fujita, K. Tanaka, K. Hirao, T. Yamamoto and I. Tanaka, *Phys. Rev. B* **75** (2007) 174443/1.

[25] C. N. Chinnasamy, A. Yang, S. D. Yoon, K. Hsu, M. D. Shultz, E. E. Carpenter, S. Mukerjee, C. Vittoria and V. G. Harris, *J. Appl. Phys.* **101** (2007) 09M509/1.

[26] V. Sepelak, A. Feldhoff, P. Heitjans, F. Krumeich, D. Menzel, F. J. Litterst, I. Bergmann and K. D. Becker, *Chem. Mater.* **18** (2006) 3057.

[27] S. Ghosh and P. Adler, *J. Mater. Chem.* **12** (2002) 511.

[28] M. Sanchez-Andujar, J. Mira, J. Rivas and M. A. Senaris-Rodriguez, *J. Magn. Magn. Mater.* **263** (2003) 282.

[29] F. Prado and A. Manthiram, *J. Solid State Chem.* **158** (2001) 307.

[30] T. Hosomi, H. Suematsu, H. Fjellvag, M. Karppinen and H. Yamauchi, *J. Mater. Chem.* **9** (1999) 1141.

[31] M. Karppinen, H. Yamauchi, T. Hosomi, H. Suematsu and H. Fjellvag, *J. Low Temp. Phys.* **117** (1999) 843.

[32] H. Yamauchi, M. Karppinen, T. Hosomi and H. Fjellvag, *Physica C* **338** (2000) 38.

[33] R. V. Shpanchenko, E. V. Antipov and L. M. Kovba, *Mater. Sci. Forum* **133-136** (1993) 639.

[34] K. Toda, Y. Kameo, S. Kurita and M. Sato, *Bull. Chem. Soc. Jpn.* **69** (1996) 349.

[35] D. Pelloquin, J. Hadermann, M. Giot, V. Caignaert, C. Michel, M. Hervieu and B. Raveau, *Chem. Mater.* **16** (2004) 1715.

[36] M. Seppanen and M. H. Tikkanen, *Acta Chem. Scand.* **A30** (1976) 389.

[37] S. N. Ruddlesden and P. Popper, *Acta Cryst.* **10** (1957) 538.

[38] P. D. Battle, J. C. Burley, D. J. Gallon, C. P. Grey and J. Sloan, *J. Solid State Chem.* **177** (2004) 119.

[39] M. Caldes, C. Michel, T. Rouillon, M. Hervieu and B. Raveau, *J. Mater. Chem.* **12** (2002) 473.

[40] M. Al-Mamouri, P. P. Edwards, C. Greaves and M. Slaski, *Nature* **369** (1994) 382.

[41] Z. Hiroi, N. Kobayashi and M. Takano, *Nature* **371** (1994) 139.

[42] C. Q. Jin, X. J. Wu, P. Laffez, T. Tatsuki, T. Tamura, S. Adachi, H. Yamauchi, N. Koshizuka and S. Tanaka, *Nature* **375** (1995) 301.

[43] G. S. Case, A. L. Hector, W. Levason, R. L. Needs, M. F. Thomas and M. T. Weller, *J. Mater. Chem.* **9** (1999) 2821.

[44] F. Galasso and W. Darby, *J. Phys. Chem.* **67** (1963) 1451.

[45] N. McGlothlin, D. Ho and R. J. Cava, *Mater. Res. Bull.* **35** (2000) 1035.

[46] C. S. Knee, A. A. Zhukov and M. T. Weller, *Chem. Mater.* **14** (2002) 4249.

[47] B. Kriworuschenko and V. Kahlenberg, *Cryst. Res. Technol.* **37** (2002) 958.

[48] H. W. King, K. M. Castelliz, G. J. Murphy and A. S. Rizkalla, *J. Can. Ceram. Soc.* **55** (1986) 10.

[49] J. F. Mitchell, J. E. Millburn, M. Medarde, S. Short, J. D. Jorgensen and M. T. Fernandez-Diaz, *J. Solid State Chem.* **141** (1998) 599.

[50] H. J. Rossell, P. Goodman, S. Bulcock, R. H. March, S. J. Kennedy, T. J. White, F. J. Lincoln and K. S. Murray, *Aust. J. Chem.* **49** (1996) 205.

[51] C. Brisi and M. Lucco Borlera, *Atti. Accad. Sci. Torino, Classe Sci. Fis., Mat. Nat.* **96** (1962) 805.

[52] E. M. Vogel and D. W. Johnson, *Thermochim. Acta* **12** (1975) 49.

[53] M. Takemoto, A. Katada, T. Ogawa and H. Ikawa, *J. Eur. Ceram. Soc.* **19** (1999) 1511.

[54] S. E. Dann, M. T. Weller and D. B. Currie, *J. Solid State Chem.* **92** (1991) 237.

[55] S. E. Dann, M. T. Weller, D. B. Currie, M. F. Thomas and A. D. Al-Rawwas, *J. Mater. Chem.* **3** (1993) 1231.

[56] A. L. Hector, J. A. Hutchings, R. L. Needs, M. F. Thomas and M. T. Weller, *J. Mater. Chem.* **11** (2001) 527.

[57] T. Nishi, K. Toda, F. Kanamaru and T. Sakai, *Key Eng. Mater.* **169-170** (1999) 235.

[58] K. Kuzushita, S. Morimoto and S. Nasu, *Physica B: Condensed Matter (Amsterdam, Netherlands)* **329-333** (2003) 736.

[59] C. S. Knee, M. A. L. Field and M. T. Weller, *Solid State Sci.* **6** (2004) 443.

[60] X. L. Wang, H. Sakurai and E. Takayama-Muromachi, *J. Appl. Phys.* **97** (2005) 10M519/1.

[61] J. Matsuno, Y. Okimoto, Z. Fang, X. Z. Yu, Y. Matsui, N. Nagaosa, M. Kawasaki and Y. Tokura, *Phys. Rev. Lett.* **93** (2004) 167202/1.

[62] X. L. Wang and E. Takayama-Muromachi, *Phys. Rev. B* **72** (2005) 064401/1.

[63] K. Kitayama, *J. Solid State Chem.* **131** (1997) 18.

[64] R. Flamand and R. Berjoan, *High Temp. - High Pressures* **15** (1983) 693.

[65] D. Pelloquin, N. Barrier, A. Maignan and V. Caignaert, *Solid State Sci.* **7** (2005) 853.

[66] K. Yamaura, Q. Huang and R. J. Cava, *J. Solid State Chem.* **146** (1999) 277.

[67] A. Olafsen, H. Fjellvaag and B. C. Hauback, *J. Solid State Chem.* **151** (2000) 46.

[68] C.-F. Kao and C.-L. Jeng, *Ceram. Int.* **26** (2000) 237.

[69] M. Burriel, G. Garcia, M. D. Rossell, A. Figueras, G. Van Tendeloo and J. Santiso, *Chem. Mater.* **19** (2007) 4056.

[70] G. Amow, I. J. Davidson and S. J. Skinner, *Solid State Ionics* **177** (2006) 1205.

[71] S. Tamura, *J. Phys. Soc. Jpn.* **33** (1972) 574.

[72] J. Drennan, C. P. Tavares and B. C. H. Steele, *Mater. Res. Bull.* **17** (1982) 621.

[73] Z. Zhang and M. Greenblatt, *J. Solid State Chem.* **111** (1994) 141.

[74] M. Seppanen, *Scand. J. Metall.* **8** (1979) 191.

[75] V. V. Vashuk, O. P. Ol'shevskaya and S. P. Prodan, *Inorg. Mater.* **32** (1996) 436.

[76] P. Lacorre, *J. Solid State Chem.* **97** (1992) 495.

[77] S.-H. Wei and S. B. Zhang, *Phys. Rev. B* **63** (2001) 045112/1.

[78] R. J. D. Tilley, *Understanding Solids: The Science of Materials*. Wiley, New York, 2004.

[79] S. Wibmann, V. von Wurmb, F. J. Litterst, R. Dieckmann and K. D. Becker, *J. Phys. Chem. Solids* **59** (1998) 321.

[80] F. Martignago, G. B. Andreozzi and A. Dal Negro, *Am. Mineral.* **91** (2006) 306.

[81] I. D. Fawcett, E. Kim, M. Greenblatt, M. Croft and L. A. Bendersky, *Phys. Rev. B* **62** (2000) 6485.

[82] H. Asano, J. Hayakawa and M. Matsui, *Phys. Rev. B* **56** (1997) 5395.

[83] M. V. Lobanov, S. Li and M. Greenblatt, *Chem. Mater.* **15** (2003) 1302.

[84] L. Viciu, H. W. Zandbergen, Q. Xu, Q. Huang, M. Lee and R. J. Cava, *J. Solid State Chem.* **179** (2006) 500.

[85] Y. Breard, C. Michel, M. Hervieu, F. Studer, A. Maignan and B. B. Raveau, *Chem. Mater.* **14** (2002) 3128.

[86] Z. Li, G. Li, J. Sun, Y. Wang, L. You and J. Lin, *Solid State Sci.* **8** (2006) 1035.

[87] Z. Li, G. Li, J. Sun, L. You, C.-K. Loong, Y. Wang, F. Liao and J. Lin, *J. Solid State Chem.* **178** (2005) 3315.

[88] R. Gundakaram, J. G. Lin, F. Y. Lee, M. F. Tai, C. H. Shen, R. S. Liu and C. Y. Huang, *J. Phys.: Condens. Matter* **11** (1999) 5187.

[89] J. Zhang, Q. Yan, F. Wang, P. Yuan and P. Zhang, *J. Phys.: Condens. Matter* **12** (2000) 1981.

[90] H. Zhu, X. Liu, K. Ruan and Y. Zhang, *Phys. Rev. B* **65** (2002) 104424/1.

[91] H. Zhu, X. Xu, L. Pi and Y. Zhang, *Phys. Rev. B* **62** (2000) 6754.

[92] R. K. Sahu, Q. Mohammad, M. L. Rao, S. Sundar Manoharan and A. K. Nigam, *Appl. Phys. Lett.* **80** (2002) 88.

[93] N. Sudhakar, K. P. Rajeev and A. K. Nigam, *J. Appl. Phys.* **93** (2003) 8331.

[94] R. K. Sahu, S. S. Manoharan, Q. Mohammad, M. L. Rao and A. K. Nigam, *J. Appl. Phys.* **91** (2002) 7724.

[95] Y. Onose, J. P. He, Y. Kaneko, T. Arima and Y. Tokura, *Appl. Phys. Lett.* **86** (2005) 242502/1.

[96] P. Ghigna, G. B. Barbi, G. Chiodelli, G. Spinolo, L. Malavasi and G. Flor, *J. Solid State Chem.* **153** (2000) 231.

[97] J. Hubsch, G. Gavoille and J. Bolfa, *J. Appl. Phys.* **49** (1978) 1363.

[98] C. P. Poole, Jr. and H. A. Farach, *Z. Phys. B: Condens. Matter* **47** (1982) 55.

[99] K. P. Thummer, M. P. Pandya, K. H. Jani, K. B. Modi and H. H. Joshi, *J. Mater. Sci.* **40** (2005) 5215.

[100] K. B. Modi, H. H. Joshi and R. G. Kulkarni, *J. Mater. Sci.* **31** (1996) 1311.

[101] A. A. Pandit, A. R. Shitre, D. R. Shengule and K. M. Jadhav, *J. Mater. Sci.* **40** (2005) 423.

[102] R. N. Bhowmik, R. Ranganathan and R. Nagarajan, *J. Magn. Magn. Mater.* **299** (2006) 327.

[103] W. Schiessl, W. Potzel, H. Karzel, M. Steiner, G. M. Kalvius, A. Martin, M. K. Krause, I. Halevy, J. Gal and et al., *Phys. Rev. B* **53** (1996) 9143.

[104] T. Kamiyama, K. Haneda, T. Sato, S. Ikeda and H. Asano, *Solid State Commun.* **81** (1992) 563.

[105] B. Jeyadevan, K. Tohji and K. Nakatsuka, *J. Appl. Phys.* **76** (1994) 6325.

[106] K. Tanaka, Y. Nakahara, K. Hirao and N. Soga, *J. Magn. Magn. Mater.* **131** (1994) 120.

[107] M. V. Landau, *Handbook of Porous Solids* **3** (2002) 1677.

[108] I. B. Sharma and D. Singh, *Bull. Mater. Sci.* **21** (1998) 363.

[109] A. Wold and K. Dwight, *J. Solid State Chem.* **88** (1990) 229.

[110] J. Nölte, *ICP Emission Spectrometry: A Practical Guide*. Wiley, New York, 2003.

[111] C. Engelhard, A. Scheffer, S. Nowak, T. Vielhaber and W. Buscher, *Anal. Chim. Acta* **583** (2007) 319.

[112] J. I. Langford and D. Louer, *Reports Prog. Phys.* **59** (1996) 131.

[113] R. A. Young, *The Rietveld Method*. Oxford University Press, Oxford, 1995.

[114] N. N. Greenwood and T. C. Gibb, *Mössbauer spectroscopy*. Chapman and Hall Ltd, London, 1971.

[115] P. Gütlich, *Mössbauer Spectroscopy I.* Springer, Berlin, 1975, Vol. V.

[116] A. Demourgues, A. Wattiaux, J. C. Grenier, M. Pouchard, J. L. Soubeyroux, J. M. Dance and P. Hagenmuller, *J. Solid State Chem.* **105** (1993) 458.

[117] O. H. Hansteen and H. Fjellvag, *J. Solid State Chem.* **141** (1998) 212.

[118] H. Deng, C. Dong, H. Chen, F. Wu, S. L. Jia, J. C. Shen and Z. X. Zhao, *Physica C* **313** (1999) 285.

[119] J. R. Grasmeder and M. T. Weller, *J. Solid State Chem.* **85** (1990) 88.

[120] N. Nguyen, L. Er-Rakho, C. Michel, J. Choisnet and B. Raveau, *Mater. Res. Bull.* **15** (1980) 891.

[121] N. Nguyen, F. Studer and B. Raveau, *J. Phys. Chem. Solids* **44** (1983) 389.

[122] K. Ruck, M. Sgraja, G. Krabbes, K. Dorr, K. H. Muller and M. Khristov, *J. Alloys Comp.* **306** (2000) 151.

[123] Z. Zhang and M. Greenblatt, *J. Solid State Chem.* **117** (1995) 236.

[124] G. M. Veith, R. Chen, G. Popov, M. Croft, Y. Shokh, I. Nowik and M. Greenblatt, *J. Solid State Chem.* **166** (2002) 292.

[125] J. M. Hill, B. Dabrowski, J. F. Mitchell and J. D. Jorgensen, *Phys. Rev. B* **74** (2006) 174417/1.

[126] M. Karppinen, A. Fukuoka, L. Niinisto and H. Yamauchi, *Supercond. Sci. Technol.* **9** (1996) 121.

[127] M. Karppinen, A. Fukuoka, T. Kaneko and H. Yamauchi, *Supercond. Sci. Technol.* **6** (1993) 265.

[128] M. Karppinen, A. Fukuoka, J. Wang, S. Takano, M. Wakata, T. Ikemachi and H. Yamauchi, *Physica C* **208** (1993) 130.

[129] M. Karppinen and H. Yamauchi, *Supercond. Sci. Eng.* **R26** (1999) 51.

[130] S. E. Dann and M. T. Weller, *J. Solid State Chem.* **115** (1995) 499.

[131] K. Yamaura, D. P. Young and R. J. Cava, *Phys. Rev. B* **63** (2001) 064401/1.

[132] D. Pelloquin, N. Barrier, D. Flahaut, V. Caignaert and A. Maignan, *Chem. Mater.* **17** (2005) 773.

[133] T. Motohashi, B. Raveau, V. Caignaert, V. Pralong, M. Hervieu, D. Pelloquin and A. Maignan, *Chem. Mater.* **17** (2005) 6256.

[134] N. N. Nevskii, B. N. Ivanov-Emin, N. A. Nevskaya, G. Z. Kaziev and N. V. Belov, *Doklady Akademii Nauk SSSR* **264** (1982) 857.

[135] J. Sugiyama, T. Atsumi, T. Hioki, S. Noda and N. Kamegashira, *J. Alloys Comp.* **235** (1996) 163.

[136] W. Cho, W. Ra, J. Shirakawa, M. Nakayama and M. Wakihara, *J. Solid State Chem.* **179** (2006) 3534.

[137] C. Laberty, J. Pielaszek, P. Alphonse and A. Rousset, *Solid State Ionics* **110** (1998) 293.

[138] S. Ito, H. Miyashita and N. Yoneda, *J. Cryst. Growth* **73** (1985) 167.

[139] A. C. C. Tseung and J. R. Goldstein, *J. Mater. Sci.* **7** (1972) 1383.

[140] S. Ghosh, P. M. G. Nambissan and R. Bhattacharya, *Phys. Lett. A* **325** (2004) 301.

[141] S. J. Kim, B. R. Myoung and C. S. Kim, *J. Magn. Magn. Mater.* **272-276** (2004) 2161.

[142] A. Lakshman, P. S. V. S. Rao and K. H. Rao, *Mater. Lett.* **60** (2005) 7.

[143] S. Wha Lee, S. Yong An and C. S. Kim, *J. Magn. Magn. Mater.* **226-230** (2001) 1403.